

# NEW ASSOCIATIONS OF GAMMA-RAY SOURCES FROM THE FERMI SECOND SOURCE CATALOG

FRANK K. SCHINZEL<sup>1</sup>, LEONID PETROV<sup>2</sup>, GREGORY B. TAYLOR<sup>1,3</sup>, ELIZABETH K. MAHONY<sup>4</sup>,  
 PHILIP G. EDWARDS<sup>5</sup>, YURI Y. KOVALEV<sup>6,7</sup>

(Received August 26, 2014; Accepted January 23, 2015)

## ABSTRACT

We present the results of an all-sky radio survey between 5 and 9 GHz of sky areas surrounding all unassociated  $\gamma$ -ray objects listed in the *Fermi* Large Area Telescope Second Source Catalog (2FGL). The goal of these observations is to find all new  $\gamma$ -ray AGN associations with radio sources  $>10$  mJy at 8 GHz. We observed with the Very Large Array and the Australia Telescope Compact Array the areas around unassociated sources, providing localizations of weak radio point sources found in 2FGL fields at arcmin scales. Then we followed-up a subset of those with the Very Long Baseline and the Long Baseline Arrays to confirm detections of radio emission on parsec-scales. We quantified association probabilities based on known statistics of source counts and assuming a uniform distribution of background sources. In total we found 865 radio sources at arcsec scales as candidates for association and detected 95 of 170 selected for follow-up observations at milliarcsecond resolution. Based on this we obtained firm associations for 76 previously unknown  $\gamma$ -ray AGN. Comparison of these new AGN associations with the predictions from using the WISE color-color diagram shows that half of the associations are missed. We found that 129 out of 588 observed  $\gamma$ -ray sources at arcmin scales not a single radio continuum source was detected above our sensitivity limit within the  $3\sigma$   $\gamma$ -ray localization. These “empty” fields were found to be particularly concentrated at low Galactic latitudes. The nature of these Galactic  $\gamma$ -ray emitters is not yet determined.

**Keywords:** catalogs, surveys, galaxies:active, gamma rays: general, radio continuum: general

## 1. INTRODUCTION

The Large Area Telescope (LAT) aboard the *Fermi* satellite has been continuously observing the  $\gamma$ -ray sky since August 2008. So far, this has resulted in the release of four all-sky catalogs, with a fifth one in preparation. They all have in common a significant fraction, typically  $> 30\%$ , of the detected point sources with no known counterpart at any other wavelength. To learn more about these objects we searched the radio sky in the vicinity of *every* unassociated  $\gamma$ -ray source deeper than any survey has done before to find new counterparts at other wavelengths in order to understand the nature of those currently unassociated objects.

The previous  $\gamma$ -ray experiment in orbit covered an energy range of 20 MeV – 30 GeV, slightly less in energy than that of *Fermi*/LAT (20 MeV –  $>300$  GeV). This was the Energetic Gamma-Ray Experiment Telescope (EGRET) on board the Compton-Gamma Ray Observatory (CGRO). Among the 188 point sources found by EGRET, there were 87 (46%) for which no multi-wavelength counterpart was found by cross-matching catalogs with expected  $\gamma$ -ray emitting

sources such as pulsars, blazars, or supernova remnants (Casandjian & Grenier 2008) and using other parameters such as correlated variability. This was complicated by the poor angular resolution (5–30′) and limited field-of-view ( $\sim 20^\circ$ ) of EGRET.

The latest generation of  $\gamma$ -ray space telescope, *Fermi*/LAT, provided a significant advancement for studying the  $\gamma$ -ray sky. However, despite recent efforts to identify those unassociated  $\gamma$ -ray emitters with known sources, the number of unassociated objects remains high throughout the *Fermi*-era. Fig. 1 illustrates the fraction of unassociated  $\gamma$ -ray sources for all the all-sky catalogs released so far, the revised EGRET point source catalog (EGR; Casandjian & Grenier 2008) and the *Fermi* 3-month bright source list (LBSL; Abdo et al. 2009), 11-month point-source catalog (1FGL; Abdo et al. 2010), 2-year point-source catalog (2FGL; Nolan et al. 2012), and first hard source list (1FHL; Ackermann et al. 2013). For the major catalogs, 1FGL and 2FGL, the fraction of unassociated sources has never dropped below 30%. Sources listed in LBSL and 1FHL are largely associated with bright radio-loud AGN for which catalogs are mostly complete thus the fraction of unassociated sources ( $< 20\%$ ) is partly due to this selection effect.

The  $1\text{-}\sigma$  positional uncertainty of the 2FGL catalog ranges from 8′′ to 15′ with a median value of 2.5′. Such large position errors makes close to impossible the direct association of  $\gamma$ -ray sources with optical data without considering other information (e.g. variability), since many candidates for association can be found within the  $\gamma$ -ray source localization errors. From the analysis of early EGRET data it was found that  $\gamma$ -ray emission and parsec-scale radio emission are strongly related, e.g. (Tingay et al. 1998). An early comparison of *Fermi*

Contact: fsch@unm.edu

<sup>1</sup> Department of Physics and Astronomy, University of New Mexico, Albuquerque NM, 87131, USA

<sup>2</sup> Astrogeo Center, Falls Church, VA 22043, USA

<sup>3</sup> An Adjunct Astronomer at the National Radio Astronomy Observatory.

<sup>4</sup> ASTRON, Netherlands Institute for Radio Astronomy, Postbus 2, NL-7990 Dwingeloo, the Netherlands

<sup>5</sup> CSIRO Astronomy and Space Science, PO Box 76, Epping, NSW 1710, Australia

<sup>6</sup> Astro Space Center of Lebedev Physical Institute, Profsoyuznaya 84/32, 117997 Moscow, Russia

<sup>7</sup> Max-Planck-Institut für Radioastronomie, Auf Dem Hügel 69, D-53121 Bonn, Germany

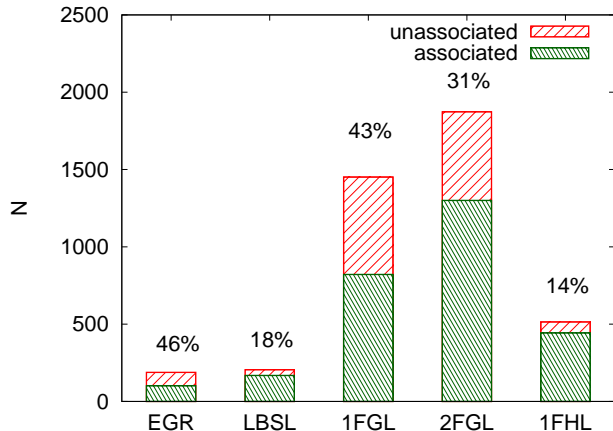


**Figure 1.** Comparison of associated and unassociated source counts of all major  $\gamma$ -ray source catalogs since EGRET.

data with radio sources from Very Long Baseline Interferometry (VLBI) observations using the 3-month list (Abdo et al. 2009) has shown that parsec-scale emission detected through VLBI is one of the best and most efficient tools to both associate *Fermi* AGN and to understand the probability of false detections (Kovalev 2009). Cross-correlation of 2FGL against a cumulative list of radio sources<sup>8</sup> detected in dedicated VLBI surveys at the Very Long Baseline Array (VLBA), Australian Long Baseline Array (LBA), and European VLBI Network (EVN) (Beasley et al. 2002; Fomalont et al. 2003; Petrov et al. 2005, 2006; Kovalev et al. 2007; Petrov et al. 2008, 2011b,a; Petrov 2012; Taylor et al. 2007; Petrov & Taylor 2011; Petrov et al. 2009; Petrov 2011, 2013; Condon et al. 2011) revealed that for the majority of 2FGL sources, 1081 out of 1872 objects have a radio counterpart with emission at milliarcsec scales brighter than 10 mJy at 8 GHz. All but three of these sources (Vela pulsar and magnetars/microquasars LSI61303 and LS5039) are active galactic nuclei (AGN). Therefore, an association of a  $\gamma$ -ray source with a compact radio source statistically implies its classification as an AGN.

Had a VLBI cumulative catalog been complete to a 10 mJy level, we would have been able to establish or rule out radio- $\gamma$  association of AGN for almost every 2FGL source. However by 2014, completeness of the all-sky for 8 GHz VLBI catalogs at the 10 mJy level has reached only 9%. Realizing the importance of radio observations for  $\gamma$ -ray associations, we launched several all-sky campaigns for observing areas within error ellipses of  $\gamma$ -ray sources without an association. The goal of these campaigns is to find all  $\gamma$ -ray AGN associations with radio sources brighter than 10 mJy at 8 GHz. This will allow us to study two interesting issues: firstly, a detailed analysis of the population of  $\gamma$ -ray AGN; and secondly, the population of remaining unassociated sources that show no radio emission.

In the following we present the results from our observing program searching for faint radio counterparts among all unassociated  $\gamma$ -ray sources listed in 2FGL. Section 2 describes the observing program and data analysis pro-

cedures for each observatory from which data were acquired. This is followed by Section 3 presenting results and the full catalog of detected radio sources together with new associations of  $\gamma$ -ray sources. This is followed by a discussion of our findings in Section 4 including a comparison with alternative association methods. A brief conclusion and summary is provided in Section 5. In the following, the radio spectral index  $\alpha$  is defined as  $S \propto \nu^\alpha$ , where  $S$  is the source flux density and  $\nu$  is the observing frequency.

## 2. OBSERVING PROGRAM

The observing program was executed in three steps. In the first step we observed with the Australia Telescope Compact Array (ATCA) and the Karl G. Jansky Very Large Array (VLA) every unassociated source using the 5–10 GHz frequency range. The telescopes were pointed to 2FGL positions. The field-of-view was defined by the area within which the total power does not drop below 20% with respect to the pointing direction. The radius from the pointing center at which a 20% drop occurs for the ATCA 22 m diameter antennas is 6.5' and 4.0' at 5.5 and 9.0 GHz respectively and for the 25 m diameter VLA antennas is 6.2' and 4.3' at 5.0 and 7.3 GHz respectively. Thus the field of views can be considered comparable. This allows imaging of the entire *Fermi*/LAT localization error ellipses, which typically have a 1- $\sigma$  semi-major axis of 2–4'. The angular resolution of our ATCA and VLA observations differs significantly: the primary synthesized beam is 0.3'' at the VLA and 40'' at the ATCA.

The second step involved only ATCA observations, where we re-observed the fields A) where sources were detected beyond the 6.5' field of view or within a side-lobe; B) where no source has been detected. In case A we pointed the array to the direction of the previous detection, in case B we used a hexagonal mosaic to double the field of view.

In a third step, we followed-up with VLBI, those sources detected with ATCA and VLA that are brighter than 10 mJy at any sub-band within 5–9 GHz. In total, 339 sources fit this criteria out of 865 detected objects in VLA and ATCA observations. We applied a flux density cutoff of 10 mJy to increase the success for a detection given limited observational resources. In addition, the probability to find a background compact radio source weaker than 10 mJy within the *Fermi* error ellipse becomes non-negligible.

We used the Australian Long Baseline Array (LBA) with baselines up to 1700 km long and the Very Long Baseline Array (VLBA) with baseline lengths up to 8,600 km. Although it is technically feasible to observe the *Fermi* fields with VLBA/LBA directly in one step, we adopted a multi-step approach for the optimal use of the resources available. We added 21 relatively bright target sources to the on-going programs, the LBA Calibrator Survey Petrov et al. (2011b) in the southern hemisphere, and 46 sources to the VLBA Calibrator Survey-7 in the northern hemisphere. These 67 objects fit the goals of these surveys. In addition we ran a dedicated VLBA observing program (VOFUS2) for observing the remaining targets with declinations  $> -30^\circ$ . A summary of all observations and their characteristic parameters is presented in Table 1.

<sup>8</sup> Available at <http://astrogeo.org/rfc>

**Table 1**  
List of observations from which results are presented.

Telescope	Config.	Code	Start (UTC)	Dur. (h)	Tune (GHz)	B/w (GHz)	#	Identifier
ATCA	H214	C2624	2012 Sep 19 10:00	29	5.5/9.0	2.0	411	AOFUS1
VLA	A	S5272	2012 Oct 26 11:19	2	5.0/7.3	1.0	41	VOFUS1A
VLA	A	S5272	2012 Nov 03 21:01	7	5.0/7.3	1.0	175	VOFUS1B
VLBA	-	BP171	2013 Feb – 2013 Aug		4.1/7.4	0.48	56	VCS7
LBA	-	V271	2013 Mar – 2013 Jun		8.2	0.13	21	LCS2
VLBA	-	S5272A	2013 Jun 08 06:12	12	7.4	0.48	33	VOFUS2A
ATCA	H214	C2624	2013 Sep 25 21:30	45	5.5/9.0	2	997	AOFUS2
VLBA	-	S5272B	2013 Oct 19 05:41	12	7.4	0.48	20	VOFUS2B
VLBA	-	S5272C	2013 Dec 02 16:55	12	7.4	0.48	33	VOFUS2C
VLBA	-	S5272D	2013 Dec 05 13:49	12	7.4	0.48	31	VOFUS2D

Column descriptors: Config. – array configuration; Code – observation proposal code; Start – start time in UTC; Dur. – duration of the observation in hours; Tune – center frequency of the tunings; B/w – bandwidth of each tuning; # – number of targets observed, in the case of AOFUS2 the number of pointings performed in mosaicking mode; Identifier – custom observation identifier.

Note: VCS7 and LCS2 campaigns had many segments. Target sources were piggy-backed onto these campaigns, so only a date range for these observations is given instead of the observation start time.

### 2.1. Very Large Array

A list of 216 target fields were observed with the VLA using a total bandwidth of 2 GHz, recording both left and right handed circular polarizations, with the integration time set to 1 s. Real-time correlation was performed using VLA’s WIDAR (Wideband Interferometric Digital ARchitecture) correlator. The instantaneous bandwidth was split into two parts, with one half centered at 5.0 GHz (4.5–5.5 GHz) and the other centered at 7.3 GHz (6.8–7.8 GHz). This provides simultaneous observation of two separate frequency bands. The observing time of 9 hours was split into two segments to be able to observe fields at all LST ranges (see Table 1). The first segment started on 2012 October 26, using 26 antennas. One antenna did not provide fringes in two of its intermediate frequencies (IFs) for the duration of the observing segment, affecting the sub-band range of 6.8–7.8 GHz only. The second segment started on 2012 November 3 and recorded with 27 antennas of the array. One of the antennas recorded with zero fringe amplitudes in two of the four IFs, providing for this antenna only half of the available bandwidth in each of the sub-bands for the entire duration of this segment. All array data were lost during correlation for the scan centered on the position of 2FGL J0423.4+5612.

At the beginning and end of each observing segment a bright flux density/bandpass calibrator was observed. In the case of the first segment these were 3C 147 and 3C 286 and, in segment two 3C 286 and 3C 48. Each target source was observed only once with a total integration time of  $\sim 45$  s. Nearby phase calibrators were added with typical integration times of 30 s each in order to be able to solve for changes in the complex gains during the target observations. For both segments the VLA was in A array configuration, providing baseline lengths from 0.68 to 36.4 km, which results in sub-arcsecond resolutions and a field of view of up to about 7 arcmin.

Initial calibration was performed using the Common Astronomy Software Applications (CASA) release 4.0.0<sup>9</sup> and the Astronomical Image Processing System<sup>10</sup> (AIPS;

Greisen 1990). Before any calibration was performed the observations were inspected for radio frequency interference (RFI) that degrade the data. Only minimal data flagging was required for the frequency range 4.5–5.5 GHz, whereas the frequency range 6.8–7.8 GHz was significantly affected by strong RFI. In order to cope with Gibbs ringing introduced by strong RFI, the data covering 6.8–7.8 GHz were smoothed using the Hann window function implemented in the CASA task `hanningsmooth`<sup>11</sup>.

After the initial flagging of RFI affected channels and times, corrections for system temperature variations measured by noise diodes installed at VLA receivers were determined and applied to the data using the tasks `gencal` (with `caltype='evlagain'`) and `applycal`. The corrected data column was then written out with the task `exportuvfits` to be imported into AIPS which provides the possibility to perform a global fringe fit, which is not yet implemented in CASA. Within AIPS the global fringe fit (task `FRING`) using the primary flux calibrator (3C 147 or 3C 286) provides correction factors to flatten the phases across the passband which are applied to the entire dataset. After applying the corrections to the dataset using AIPS tasks `CLCAL` and `SPLAT`, the data were exported from AIPS and imported back into CASA for the final calibration and imaging steps.

In this last step the VLA antenna elevation dependent gain and antenna efficiencies were corrected for. The flux densities for the primary flux calibrator were determined using the corresponding models for 3C 147 and 3C 286 which are provided in CASA<sup>12</sup>. After this the bandpass calibration was performed using the primary and secondary flux calibrators (3C 147, 3C 286, and 3C 48). Finally complex gain corrections were derived for the secondary calibrators and the flux density scale was determined. In the last step all these gain and phase corrections were applied to the entire dataset including the target fields. The resulting dataset was inspected and

<sup>9</sup> <http://casa.nrao.edu>

<sup>10</sup> <http://www.aips.nrao.edu/index.shtml>

<sup>11</sup> This function uses a Hann window to smooth the frequency channels with a weighted running average, which suppresses the oscillations introduced by the Fourier transform of a strong narrow-band RFI signal.

<sup>12</sup> Also available at: <https://science.nrao.edu/facilities/vla/data-proce>

channels around the bandpass edges were flagged.

All targeted source fields were deconvolved using the CASA task `clean`. This task uses a Clark based clean algorithm (Clark 1980), applies a  $w$ -projection needed for widefield imaging using 100 projection planes, and uses visibility weights determined according to Briggs weighting scheme (Briggs 1995). The deconvolution was run with 5000 iterations, a default loop gain of 0.1, and a flux density threshold at which to stop cleaning of 0.05 mJy corresponding to the approximate thermal noise limit. All target fields were imaged assuming a flat spectral index across the 1 GHz bandwidth. All images are then analyzed by a semi-automatic script reading images into AIPS and using the task `SAD` to identify point sources. Custom scripts in the Python programming language were developed to analyze the resulting images and point sources found. Sometimes the algorithm applied in `SAD` identifies image artifacts in the case of strong point-sources, which were manually flagged in order to retain a clean list of point sources that includes position and flux density for each of the two 1 GHz sub-bands which are used in subsequent analysis.

## 2.2. Australia Telescope Compact Array

During the first campaign with ATCA, from 2012 September 19–20, we observed 411 2FGL unassociated sources in a declination range of  $[-90^\circ, +10^\circ]$  at 5.5 and 9 GHz for 29 hours. The details of that observing campaign and results have been reported by Petrov et al. (2013). We detected a total of 424 point sources.

In a second 45 hour ATCA campaign on 2013 September 25–28 we re-observed sources that were detected at 5 GHz, but were not detected at 9 GHz, and had position offsets exceeding the full-width at half maximum of the 9 GHz beam in the first ATCA campaign. This included also sources that were detected at the edge of the beam or within a sidelobe. In addition, 130 sources that were not detected in 2012 were re-observed using the six-element mosaic mode allowing detection of all radio sources brighter than 1 mJy located within the entire 95% probability ellipse of the 2FGL localization.

Both the 2012 and 2013 observations were conducted in array configuration H214 with baselines ranging from 82–247 m between the inner five antennas and  $\sim 4.4$  km between the sixth, CA06, and the inner antennas. Observations were recorded simultaneously in two bands centered at 5.5 and 9.0 GHz with a bandwidth of 2 GHz each and in both linear polarizations.

## 2.3. Very Long Baseline Array

Follow-up observations of 149 targets selected from the VLA and ATCA survey above  $-30^\circ$  declination were conducted with the VLBA. Sources with VLA flux densities greater than 20 mJy were added to the list of targets of the VLBA Wide-Field Calibrator Survey-7 (VCS7, L. Petrov, paper in preparation). These observations were scheduled in the so-called filler mode by the array operator using software with a web front-interface that we provided. The array operator scheduled segments with blocks 3–8 hours long during periods of time when one or two stations were down due to technical problems or suffered from bad weather that impeded high-priority projects. The goal of the VCS7 project was to find

more compact radio sources, to determine their positions with sub-mas accuracies, and to obtain snap-shot images. Observations of strong pre-selected targets fit the goal of that campaign. VCS7 observations were taken in right circular polarization at two wings of the C-band receiver: at 4.128–4.608 and 7.392–7.872 GHz simultaneously. Each subband was recorded in 8 IFs of 32 MHz each with some gaps. The aggregate recording rate was 2 Gbps. Among 94 candidates inserted in the observation queue, 48 were observed in one scan 180 s long each, and 29 were detected. Sources that have not been detected have a correlated flux density weaker than 12 mJy.

The remaining 101 sources with declinations  $> -30^\circ$  and flux densities  $> 10$  mJy were observed in a dedicated campaign S5272 in 2013 June–December in four 12 hour long segments (see Table 1). These observations used only the upper sub-band (7.392–7.872 GHz) with the same intermediate frequency setup as in VCS7, but ran in the dual polarization mode. This lowered the detection limit by 40%. Each target was observed in 3–4 scans of 210 seconds long each, along with a suitable phase calibrator located within  $2-3^\circ$ .

The data were correlated with the NRAO’s DiFX software correlator in Socorro, NM (Deller et al. 2011). The spectral resolution of the output visibility function, 0.25 MHz, and duration of accumulation periods, 0.25 s, was sufficient to detect sources within  $1'$  of the field center. Fringe fitting over the entire search window was performed with *PIMA* software<sup>13</sup>. The result of fringe fitting, group delays and the visibilities averaged over frequency and over 20 s long time intervals were exported for post-processing with VTD/Post-Solve<sup>14</sup> and Difmap data processing software for absolute astrometry analysis and imaging respectively. Astrometric analysis consists of two steps: initial and final. During the initial step a parametric model that includes coordinates of target sources, positions of stations, and the clock function in residual path delay represented as a B-spline of the 1st degree, was adjusted to group delays using least squares fitting. At first, only the observations with the probability of a false detection of less than 0.01 were used. For this experiment observations with the signal-to-noise ratio (defined as the ratio of the fringe amplitude to the average value of noise) greater than 5.76 satisfied that criteria. We ran an iterative procedure for outlier elimination. Observations with residual group delay exceeding  $4\sigma$  were discarded. Sources with less than four remaining observations were considered non-detections. We have detected a little over one half of the sources from our S5272 campaign: 58 out of 101. The procedure of fringe fitting with a narrow search window, 2 ns over group delay and  $10^{-12}$  over delay rate, was repeated for detected sources. Then the step of initial astrometric analysis was repeated. The final astrometric analysis was done by running a global least square solution with all astrometry/geodesy observations acquired since 1980 April 1 through 2014 April 7 including VCS7 and S5272 experiments, a total of 10.7 million observations. In the case of astrometric/geodetic analysis an observation refers to a single group delay obtained from one scan (pointing) of one baseline. Then the observations of detected sources,

<sup>13</sup> See <http://astrogeo.org/pima>

<sup>14</sup> See <http://astrogeo.org/vtd>

except those which were marked as outliers during an astrometric solution, were averaged over frequencies within an IF and over 20 seconds and used for hybrid imaging with Difmap. The post-processing procedure is described in more detail in Petrov et al. (2011a).

Astrometric accuracy for all but two sources was in the range of 0.2–2 mas, with a median uncertainty of 0.4 mas. The image rms was in the range 70–120  $\mu$ Jy and it was limited by thermal noise. The overall baseline-based detection limit was around 8 mJy.

#### 2.4. Long Baseline Array

For sources with declinations below  $-30^\circ$  we added 21 objects to the on-going LBA Calibrator Survey (LCS) campaign (Petrov et al. 2011b). In the LCS campaign we observed at 8.200–8.520 GHz, but using different stations equipped with heterogeneous data acquisition systems recording at different bandwidth due to hardware limitations. The recording rate ranged from 256 to 1024 Mbps for different stations. Target sources were observed in two scans of 240 s long each. The astrometric analysis performed was similar to that used in the VCS7 and S5272 campaigns, except that it involved an additional step of resolving group delay ambiguity with a spacing of 3.9 ns using a highly sophisticated algorithm. Since it is problematic to produce high quality snap-shot images using the LBA network, we resorted to evaluation of median correlated flux densities in three ranges of projected baseline lengths: 0–6 M $\lambda$ , 6–25 M $\lambda$ , 25–50 M $\lambda$ . The details of analysis of LBA observations can be found in Petrov et al. (2011b).

Of 21 sources observed on 2013 March 15 and 2013 June 15, we have detected 8 objects. The detection limit was  $\sim 10$  mJy. Thus, in three VLBI campaigns we have to date observed half of the candidates for association that were found and detected 95 sources, i.e., 56%. We plan to observe the remaining 159 objects in the near future.

### 3. RESULTS

#### 3.1. Radio Source Catalog

For ATCA the root-mean-squared (rms) of image noise was found to be in the range of 0.15–0.25 mJy beam $^{-1}$ , with a typical full width at half-maximum (FWHM) size of the restored beam of 35'' at 5 GHz and 20'' at 9 GHz. The detection limit was determined to be 1.8 mJy for sources in the center of the field of view and 9 mJy at the edge of the 5.5 GHz field of view, at 6.5'. In the case of the VLA observations, the image noise rms was found to be in the range of 0.18–0.01 mJy beam $^{-1}$  with a median value of 0.08 mJy beam $^{-1}$ , a factor of two smaller than that of ATCA. The typical FWHM size of the restored beam was 24'' at 5.0 GHz and 7'' at 7.3 GHz providing a significantly higher resolution and a higher rejection of extended sources than ATCA. The  $2\sigma$  detection limit for the VLA observations was determined to be 0.37 mJy for sources in the center of the field of view and 1.1 mJy at the edge of the 5.0 GHz field of view, at 6.5'. Sources with evidence of extended emission were flagged accordingly. The radio sources found in the ATCA observation at 5.5 and 9.0 GHz around 2FGL J1634.4-4743c were not included in the following analysis due to indications of the presence of an extended source structure and confu-

sion from the Galactic plane.

The detected point source candidates for both the VLA and ATCA were combined into a single uniform dataset and the positions determined at different frequencies were spatially cross-matched in order to identify detections of the same object across the observed bands. For the 35 fields that were observed both with ATCA and the VLA, ATCA information was only used if no point source was detected by the VLA within 20'' of the  $\gamma$ -ray localization. ATCA observations are sensitive to larger angular scale structures as compared to the VLA and have thus a higher chance of detecting extended Galactic sources. These fields were also used to check for systematic differences between ATCA and VLA observations. We found good agreement between the detected point sources for most of those fields. However, for some sources the VLA counterpart showed fainter emission indicating a significant component of extended emission. There were also a small number of weak point sources only detected by either ATCA or VLA but not by both. Since ATCA is more sensitive to larger scale emission, due to shorter baselines, those sources added by ATCA are most likely related to large scale radio sources rather than to compact sources which are primarily targeted. Nevertheless, we have included those detections in the combined candidate catalog. To summarize, we have detected a total of 1,268 unique point sources with connected radio interferometers in 588 fields selected from the 2FGL catalog. Among those were 325 observed with the VLA and 943 observed with ATCA, where 58 sources were found in fields co-observed by the VLA and ATCA.

All radio point sources found were cross-matched against the NRAO VLA Sky Survey (NVSS: Condon et al. 1998), Sydney University Molonglo Sky Survey (SUMSS, version 2.1 of 2012 February 16: Bock et al. 1999; Mauch et al. 2003), the Molonglo Galactic Plane Survey 2nd Epoch (MGPS-2: Murphy et al. 2007), the Supercosmos database (Hambly et al. 2001), and the Wide-field Infrared Survey Explorer (WISE) catalog<sup>15</sup> (ALLWISE, November 13, 2013 Wright et al. 2010; Mainzer et al. 2011), which combines the data from the WISE cryogenic and post-cryogenic survey phases providing the most comprehensive view of the full mid-infrared sky currently available.

The NVSS catalog is derived from VLA observations at 1.4 GHz, the SUMSS and MGPS-2 catalogs are derived from observations at 0.843 GHz with the Molonglo Observatory Synthesis Telescope. These catalogs have similar resolutions of  $\sim 40''$  and are complementary to each other, as they cover different areas of the sky. We searched for optical counterparts using the Supercosmos database (Hambly et al. 2001). This database contains the digitized sky survey plates taken with the UK Schmidt telescope and is complete down to a B magnitude of B=22. Radio sources within  $10^\circ$  of the Galactic plane (719 objects) were excluded in the optical cross-matching due to increased dust extinction and contamination of foreground stars at low Galactic latitudes. The ALLWISE catalog includes point-like and resolved objects detected at infrared wavelengths between 3.4 and 22  $\mu$ m with a corresponding angular resolution between

<sup>15</sup> <http://wise2.ipac.caltech.edu/docs/release/allwise/>

Table 2

The first 8 rows of 148 objects that were detected at 5.0/5.5 and/or 7.3/9.0 GHz within 2.7 arcmin of the 2FGL counterpart localization. Table 2 is published in its entirety in the electronic edition. A portion is shown here for guidance regarding its form and content.

IAU name	2FGL name	F	$\alpha$	$\delta$	$\Delta\alpha$	$\Delta\delta$	$F_5$	$F_7$	$F_9$	$\Delta F_5$	$\Delta F_7$	$\Delta F_9$	$Sp_5$	$Sp_9$	$\Delta Sp_5$	$\Delta Sp_9$	$Sp$	$\Delta Sp$	$D$	$N\sigma$	Camp.
			(h) (min) (s)	( $^{\circ}$ ) ( $'$ ) ( $''$ )	( $''$ )	( $''$ )	(mJy)	(mJy)	(mJy)	(mJy)	(mJy)	(mJy)	(14)	(15)	(16)	(17)	(18)	(19)	(20)	(21)	(22)
(1)	(2)	(3)	(4)	(5)	(6)	(7)	(8)	(9)	(10)	(11)	(12)	(13)	(14)	(15)	(16)	(17)	(18)	(19)	(20)	(21)	(22)
J0002+6219	J0002.7+6220		00 02 53.52	+62 19 17.03	0.050	0.050	3.47	1.78		0.19	0.20						-1.77	0.33	1.6	0.8	V1
J0004+2206	J0004.2+2208		00 04 07.36	+22 06 15.76	0.050	0.050	1.86	1.38		0.18	0.20						-0.79	0.46	2.4	0.6	V1
J0039+4330	J0039.1+4331		00 39 01.86	+43 30 29.35	0.050	0.050	1.70	1.14		0.20	0.16						-1.06	0.48	1.5	0.6	V1
J0039+433A	J0039.1+4331	f	00 39 08.16	+43 30 14.63	0.050	0.050	6.46	5.99		0.20	0.20						-0.20	0.12	1.4	0.5	V1
J0102+0944	J0102.2+0943	f	01 02 17.11	+09 44 09.54	0.050	0.050	14.77	14.72		0.18	0.17						-0.01	0.04	1.2	0.4	V1
J0103+1323	J0103.8+1324	f	01 03 45.74	+13 23 45.25	0.050	0.050	19.79	17.62		0.15	0.15						-0.31	0.03	0.8	0.3	V1
J0116-6153	J0116.6-6153	f	01 16 19.70	-61 53 43.00	0.500	0.799	33.50		30.50	0.30		0.60	-0.04	-0.30	0.05	0.20	-0.19	0.04	2.7	1.2	A1
J0143-5845	J0143.6-5844	f	01 43 47.45	-58 45 51.80	0.500	0.799	24.00		22.30	0.20		0.40	-0.18	-0.47	0.06	0.17	-0.15	0.04	1.5	1.2	A1

Column description: (1) IAU conforming name; (2) Name listed in 2FGL catalog; (3) flags: e for extended source, f for flat spectrum source; (4) right ascension coordinate of radio source; (5) declination coordinate of radio source; (6) error in right ascension; (7) error in declination; (8) 5.0/5.5 GHz flux density; (9) 7.3 GHz flux density; (10) 9.0 GHz flux density; (11)-(13) corresponding flux density errors; (14) spectral index from 5.5 GHz band; (15) spectral index from 9.0 GHz band only; (16)-(17), (19) spectral index errors; (18) spectral index between 5.0/5.5 and 7.2/9.0 GHz bands; (20) distance between radio and  $\gamma$ -ray localization; (21) normalized separation between radio and  $\gamma$ -ray localization, i.e. ratio of the separation to the  $1\sigma$  uncertainty; (22) observing campaign: V1 - VLA, A1/A2 - ATCA.

6.1 and  $12''$ . We used a search radius of  $20''$  to find counterparts in the NVSS, SUMSS, and MGPS-2 catalogs,  $3.5''$  to search for optical counterparts and  $7''$  for matching to an ALLWISE object. We obtained 687 matches with the ALLWISE catalog, 222 matches with the SuperCOSMOS database, 610 matches with NVSS, 116 matches with SUMSS, and 161 matches with MGPS-2. There were 47 objects that had both a counterpart in NVSS and MGPS-2 or SUMSS.

The radio spectral index was determined for all detected sources where possible. For sources detected at both sub-bands independently, we determined spectral indices between 5.0/5.5 and 7.3/9.0 GHz directly from their flux densities. For ATCA detections, the 2 GHz bandwidths at 5.5 and 9.0 GHz were divided into 2048 spectral channels, allowing determination of spectral indices even for objects that were found only in one sub-band. No spectral index was determined for objects detected only in one sub-band of a VLA observation since no multi-frequency techniques were applied in the analysis due to the reduced bandwidth per sub-band of 1 GHz. As a note of caution, spectral indices determined between both sub-bands in comparison to those determined from only the low-sub-band do not necessarily match. The reason for this can be systematic errors affecting the estimates in different ways and intrinsic source spectra deviating from that of a power law. For the following discussion we only include spectral indices of sources that were detected in both sub-bands with either the VLA or ATCA.

The final list of 865 sources can be split into four different categories:

(i) **Category I:** We detected 148 objects at arcsec scales in the 5.0/5.5 and 7.3/9.0 GHz sub-bands within  $2.7'$  of the localization of the 2FGL object, which also corresponds to the pointing direction of the radio observations with the exception of fields observed using mosaicking. Among those sources 125 were detected at both sub-bands. For all sources in this category we provide the following information in Table 2:  $\gamma$ -ray source name; IAU name of the detected radio source; J2000 coordinates followed by  $1\sigma$  uncertainties in arcsec; flux densities at 5.0/5.5 and 7.3/9.0 GHz in mJy corrected for beam attenuation, followed by their standard devia-

tions, spectral indices, and distance of the source from the pointing direction. Source flags are listed in column 3, where ‘e’ stand for a source that is extended and ‘f’ is listed if the source has a spectral index flatter than  $-0.5$ .

(ii) **Category II:** We detected 501 objects at arcsec scales in the 5.0/5.5 GHz and/or 7.3/9.0 GHz sub-bands between 2.7 and  $6.5'$  of the pointing direction and within  $3\sigma$  of the  $\gamma$ -ray localization. Similarly to Table 2 we list the Category II sources in Table 3.

(iii) **Category III:** We detected 216 objects at arcsec scales that were found beyond  $6.5'$  from the 2FGL localization but were within the  $3\sigma$  confidence of the 2FGL  $\gamma$ -ray source localization. These objects are listed in Table 4. Flux density values provided in this table are to be considered lower limits due to beam attenuation, consequently no errors for those values are provided.

In addition we have detected 403 arcsec-scale sources outside of the  $3\sigma$  error ellipse of the 2FGL  $\gamma$ -ray source localization (**Category IV**). This list of sources was not tabulated since they are not considered to be candidates for association with a  $\gamma$ -ray source. A fill value of  $-9.9$  in all tables indicates a lack of information. In the case where there is a flux density listed but the corresponding error is listed with a value of  $-9.9$  then the flux density value is to be treated as a lower limit. The presence of additional associations for 2FGL objects reported in the literature since the release of the 2FGL catalog are marked with a flag. The convention for the IAU names was applied to the list of all sources regardless of the category defined above. It thus allows unique identification of radio point sources using this identifier across all category tables. A letter replaces the last digit of the IAU name if there were multiple separate radio sources sharing the same name. All sources were sorted in right ascension order, then names were checked for double entries. If identical names were found, we replace the 10th digit with a letter A. If the 10th letter of the previous source was A, then change the name to B, and so forth.

In Table 5 we list multiwavelength counterpart information for sources listed in Tables 2, 3, and 4 using IAU name as the unique identifier. If the source was associated with an object from either NVSS, SUMSS or MGPS-2 catalogs, its flux density at 1.4 GHz (NVSS) or 0.843 GHz (SUMSS and MGPS-2) is listed along with the

**Table 3**

The first 8 rows of 501 objects that were detected at 5.0/5.5 GHz and/or 7.3/9.0 GHz between 2.7 and 6.5 arcmin of the 2FGL counterpart localization. Table 2 is published in its entirety in the electronic edition. A portion is shown here for guidance regarding its form and content.

IAU name	2FGL name	F	$\alpha$	$\delta$	$\Delta\alpha$	$\Delta\delta$	$F_5$	$F_7$	$F_9$	$\Delta F_5$	$\Delta F_7$	$\Delta F_9$	$Sp_5$	$Sp_9$	$\Delta Sp_5$	$\Delta Sp_9$	$Sp$	$\Delta Sp$	$D$	$N\sigma$	Camp.
			(h)	(min) (s)	( $^{\circ}$ ) ( $'$ ) ( $''$ )	( $''$ )	( $''$ )	(mJy)	(mJy)	(mJy)	(mJy)	(mJy)	(14)	(15)	(16)	(17)	(18)	(19)	(20)	(21)	(22)
(1)	(2)	(3)	(4)	(5)	(6)	(7)	(8)	(9)	(10)	(11)	(12)	(13)	(14)	(15)	(16)	(17)	(18)	(19)	(20)	(21)	(22)
J0006+6823	J0007.7+6825c		00 06 35.75	+68 23 20.16	0.050	0.050	14.07												6.4	1.7	V1
J0014-0512	J0014.3-0509	f	00 14 33.85	-05 12 48.80	11.999	48.802	3.20			3.50				0.40					5.1	1.4	A1
J0031+0724	J0031.0+0724	f	00 31 19.71	+07 24 53.61	0.050	0.050	6.42	5.88		0.25	0.32						-0.23	0.18	3.4	1.5	V1
J0039+4332	J0039.1+4331		00 39 22.81	+43 32 52.21	0.050	0.050		2.10			0.34								3.1	1.2	V1
J0049-6344	J0048.8-6347	f	00 49 32.92	-63 44 11.39	2.531	4.723	1.70			0.40			-3.00		1.29				5.7	2.0	A2
J0116-6150	J0116.6-6153		01 16 56.83	-61 50 12.50	0.900	1.102	7.10		5.40	0.40			1.20	-1.04	0.29		-0.56	0.47	3.5	1.8	A1
J0116-6156	J0116.6-6153	f	01 16 43.97	-61 56 53.30	0.601	0.799	17.50		15.80	0.40			1.30	-0.31	0.14		-0.21	0.17	3.7	1.9	A1
J0152+8557	J0158.6+8558		01 52 48.19	+85 57 03.50	0.050	0.050	10.67												6.3	1.6	V1

Column description: (1) IAU conforming name; (2) Name listed in 2FGL catalog; (3) flags: e for extended source, f for flat spectrum source; (4) right ascension coordinate of radio source; (5) declination coordinate of radio source; (6) error in right ascension; (7) error in declination; (8) 5.0/5.5 GHz flux density; (9) 7.3 GHz flux density; (10) 9.0 GHz flux density; (11)-(13) corresponding flux density errors; (14) spectral index from 5.5 GHz band; (15) spectral index from 9.0 GHz band only; (16)-(17), (19) spectral index errors; (18) spectral index between 5.0/5.5 and 7.2/9.0 GHz bands; (20) distance between radio and  $\gamma$ -ray localization; (21) normalized separation between radio and  $\gamma$ -ray localization, i.e. ratio of the separation to the 1- $\sigma$  uncertainty; (22) observing campaign: V1 - VLA, A1/A2 - ATCA.

**Table 4**

The first 8 rows of 216 objects that were detected outside of the 6.5 arcmin and the were within the 99% position uncertainty of the 2FGL counterpart localization. Table 4 is published in its entirety in the electronic edition. A portion is shown here for guidance regarding its form and content.

IAU name	2FGL name	F	$\alpha$		$\delta$		$\Delta\alpha$	$\Delta\delta$	$F_5$	$F_7$	$F_9$	$D$	$N\sigma$	Camp.
			(h)	(min)	(s)	( $^{\circ}$ )	( $'$ )	( $''$ )	( $''$ )	(mJy)	(mJy)	(mJy)	( $'$ )	(13)
(1)	(2)	(3)	(4)	(5)	(6)	(7)	(8)	(9)	(10)	(11)	(12)	(13)	(14)	(15)
J0001+6331	J2358.9+6325		00 01 00.63	+63 31 49.49	0.050	0.050	11.58					15.1	2.1	V1
J0039+4336	J0039.1+4331		00 39 28.71	+43 36 51.13	0.050	0.050	19.92					6.5	2.5	V1
J0047-6344	J0048.8-6347	f	00 47 40.59	-63 47 39.37	0.990	1.768	3.40				2.20	7.9	2.7	A2
J0103+1319	J0103.8+1324		01 03 20.99	+13 19 35.32	0.050	0.050	16.53					8.1	2.8	V1
J0125-2325	J0124.6-2322	f	01 25 02.21	-23 25 52.90	0.270	0.241	13.50				7.40	6.9	2.8	A2
J0126+6335	J0128.0+6330		01 26 40.47	+63 35 28.21	0.050	0.050				17.64		10.3	1.8	V1
J0133-4414	J0133.4-4408	f	01 33 06.40	-44 14 21.41	0.068	0.083	45.70				41.60	6.9	2.9	A2
J0149+8601	J0158.6+8558		01 49 34.23	+86 01 14.81	0.050	0.050				12.77		10.1	2.6	V1

Column description: (1) IAU conforming name; (2) Name listed in 2FGL catalog; (3) flags: e for extended source, f for flat spectrum source; (4) right ascension coordinate of radio source; (5) declination coordinate of radio source; (6) error in right ascension; (7) error in declination; (8) 5.0/5.5 GHz flux density upper limit; (9) 7.3 GHz flux density upper limit; (10) 9.0 GHz flux density upper limit; (11) distance between radio and  $\gamma$ -ray localization; (12) normalized separation between radio and  $\gamma$ -ray localization, i.e. ratio of the separation to the 1- $\sigma$  uncertainty; (13) observing campaign: V1 - VLA, A1/A2 - ATCA.

**Table 5**

Possible counterparts from previous radio source catalogs, the ALLWISE catalog, and the Supercosmos database for radio sources found in Cat I, II, and III. Table 5 is published in its entirety in the electronic edition. A portion is shown here for guidance regarding its form and content.

IAU name	$F_1$	$C_1$	$I_1$	$I_w$	$D_{\text{opt}}$	$\alpha_{\text{opt}}$	$\delta_{\text{opt}}$	B	R	$C_{\text{opt}}$				
	(mJy)				( $''$ )	(h)	(min)	(s)	( $^{\circ}$ )	( $'$ )	( $''$ )	(Mag.)	(Mag.)	
(1)	(2)	(3)	(4)	(5)	(6)	(7)	(8)	(9)	(10)	(11)				
J0001+6331	7.3	J000100+633152	N	J000100.72+633150.9			-	-						-
J0002+6219	12.7	J000253+621917	N	J000253.17+621917.6			-	-						-
J0004+2206		-	-	J000407.36+220615.6	0.4	00 04 07.39	+22 06 15.7	21.1	20.0	2				
J0008+6837	264.4	J000833+683721	N	J000833.39+683722.1			-	-						-
J0014-0512	4.3	J001433-051244	N	J001433.87-051249.7			-	-						-
J0031+0724	11.6	J003119+072456	N	J003119.71+072453.4	0.5	00 31 19.69	+07 24 53.2	19.3	19.1	2				
J0031-5511	18.1	J003156-551149	S	J003156.87-551145.1			-	-						
J0031-5521	381.2	J003102-552107	S	J003102.47-552104.3			-	-						-

Column description: (1) IAU conforming name; (2) Radio counterpart flux density listed in NVSS/SUMSS/MGPS-2; (3) Name of counterpart NVSS/SUMSS/MGPS-2, if there are matching counterparts found in multiple catalogs, the name of the NVSS counterpart is listed; (4) catalogs in which radio counterparts were found N = NVSS, M = MGPS-2, and S = SUMSS; (5) Name of ALLWISE counterpart; (6) distance of an optical counterpart from the  $\gamma$ -ray localization; (7),(8) position of optical counterpart right ascension and declination; (9) optical B magnitude; (10) optical R magnitude; (11) optical classification '1' - extended morphology, '2' - stellar or point-like object.



corresponding source identifier in that catalog. In cases where both a NVSS and SUMSS or MGPS-2 source is associated, the flux density value and name of only the NVSS source is listed. In this case the presence of an additional association over that of NVSS is indicated in a separate column. If the source had an optical counterpart in Supercosmos, the optical position, B and R magnitude and classification is listed. This classification is based on the optical morphology where ‘1’ represents an extended morphology and ‘2’ indicates a stellar or point-like object. If the source was associated with a WISE object, its WISE source ID is listed as well.

The spectral index of category I and II objects was determined for 304 objects and their distribution is visualized in Fig. 2. The distribution is similar for both ATCA and VLA with a sharp rise in source counts with spectral indices  $> -2.0$ . For Cat I objects 77 out of 137 are considered flat spectrum with a spectral index above  $-0.5$ . For the combined distribution the split between flat and steep spectrum sources is almost exactly 50/50, with 153 steep spectrum and 151 flat spectrum sources. The flux density distribution of category I and II objects found is shown in Fig. 3. The source counts drop slightly below 2.5 mJy, thus given the expected source count distribution we can assume the observations to be complete to a flux density level of 2.5 mJy. The ATCA observations find a factor of four more sources at 5.5 and 9.0 GHz with flux densities above 50 mJy. This can be explained by the shallowness of existing multi-frequency catalogs in the southern hemisphere with respect to the northern hemisphere. This causes many radio sources in the northern hemisphere to be already associated with  $\gamma$ -ray sources therefore creating a bias toward the southern hemisphere. The overall flux density distribution is comparable to that of the extrapolated and scaled log  $N$ –log  $S$  distribution observed for compact sources ( $\leq 50$  mas) found across the entire sky between 0.18 and 5.0 Jy at 8 GHz (see also Petrov et al. 2013). No correlation was found between radio flux density and spectral index for category I objects. The source distribution in Galactic latitude between flat spectral index and other types of detected radio sources with a steep or no spectral index at 5.0/5.5 GHz is comparable, see Fig. 4. The distribution of sources with respect to Galactic latitude clearly shows an overabundance of detected sources around the Galactic plane. Most AGN surveys focus on regions outside of the Galactic plane thus the Second Catalog of Active Galactic Nuclei detected by the Fermi Large Area Telescope requires Galactic latitudes  $> |10|^\circ$  (Ackermann et al. 2011). Additionally, catalogs of other types of  $\gamma$ -ray emitting sources, namely supernova remnants and pulsars have a bias toward the Galactic plane but neglect other parts of the sky. Looking at the distribution of unassociated  $\gamma$ -ray sources reported in 2FGL and that were observed with VLA and ATCA, we find that 54% fall within  $|b| < 10^\circ$ .

### 3.2. Fields with no detections

We found that 129 out of the 589 unassociated  $\gamma$ -ray sources observed did not show a single compact radio source within their  $3\sigma$  confidence localization above the detection limits of our observations of  $\sim 1$ –2 mJy. In 10 of those pulsed emission was detected, one was related to emission from a Supernova Remnant, and one was re-

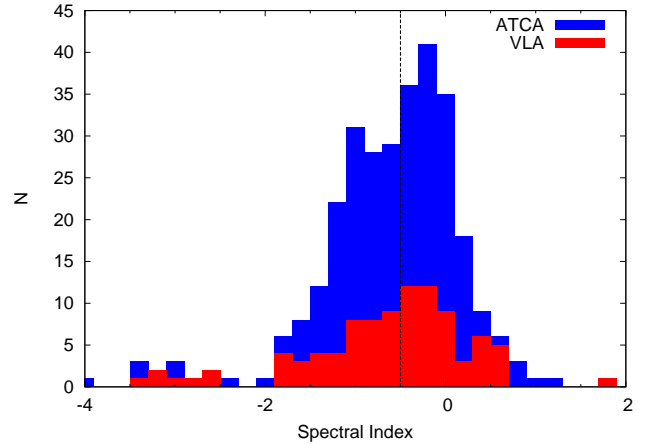


**Figure 2.** Stacked histogram of radio spectral indices of category I and II objects found by ATCA and VLA between the frequencies 5.5 and 9.0 GHz and 5.0 and 7.3 GHz respectively. The vertical dashed line indicates the  $-0.5$  value above which sources are considered flat spectrum.

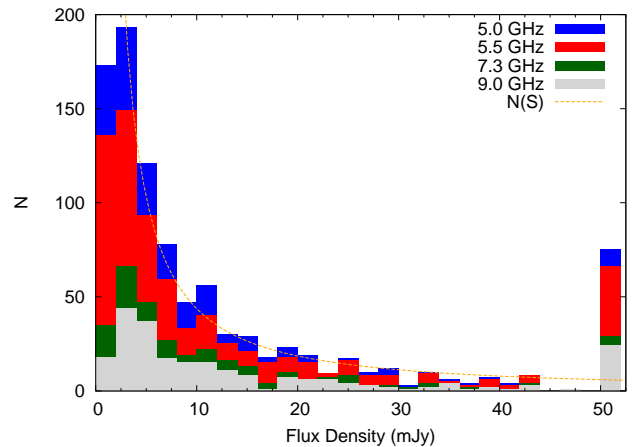


**Figure 3.** Stacked histogram of the flux density distribution of all radio sources found within 6.5 arcmin of the  $\gamma$ -ray localization (category I and II). The frequencies at 5.0 and 7.3 GHz represent the VLA observations, while 5.5 and 9.0 GHz represent the data from ATCA observations. The last bin aggregates the number of sources found above 50 mJy. The orange dashed line represents the expected flux density distribution of compact sources extrapolated and scaled from 8 GHz observations of correlated flux density of regions smaller than 50 mas.

lated to emission from a Low Mass X-ray binary (see Section 3.4). The positions and rms sensitivity limits of the remaining 117 “empty” fields are listed in Table 6. No flag indicates that no point source was detected in both sub-bands within the entire field of view, a ‘\*’ flag indicates that at least one point source was detected outside of the  $3\sigma$  2FGL confidence localization error and ‘e’ indicates the possible presence of an extended source near the center of the field.

The distribution of the empty fields in Galactic latitude  $|b|$  is shown in Fig. 5 together with the distributions of  $\gamma$ -ray loud AGN and the known class of  $\gamma$ -ray loud pulsars, namely millisecond pulsars (pulse period  $< 0.01$  s) and young pulsars (age  $< 20,000$  years). Most of the empty fields are found along the Galactic plane with 25%



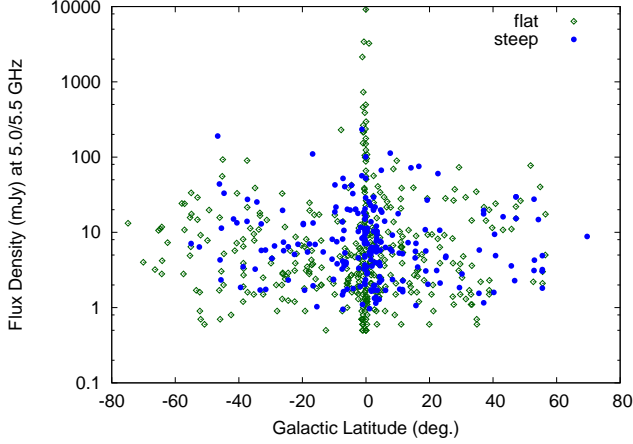


**Figure 4.** Flux density dependence of detected sources at 5.0/5.5 GHz in categories I and II with respect to Galactic latitude. Flat-spectrum ( $\alpha > -0.5$ ) sources are shown by green hollow squares and steep-spectrum sources ( $\alpha < -0.5$ ) are shown by filled blue circles.

falling within  $\pm 1^\circ$  and 67% falling within  $\pm 10^\circ$  of the Galactic plane. The 1-100 GeV  $\gamma$ -ray fluxes of the empty fields range between  $2.3 \cdot 10^{-10}$  and  $1.6 \cdot 10^{-8} \text{ ph cm}^{-2} \text{ s}^{-1}$  with a mean value of  $2.7 \cdot 10^{-9} \text{ ph cm}^{-2} \text{ s}^{-1}$ . The average  $\gamma$ -ray photon spectral index is  $2.34 \pm 0.29$  and only two fields had a photon index of less than 1.8. No correlation was found between the  $\gamma$ -ray fluxes and photon indices of empty fields. The general population of unassociated  $\gamma$ -ray sources from 2FGL has 67% concentrated at  $|b| < 10^\circ$  and 26% at  $|b| < 1^\circ$ . Comparing the distribution of empty fields in Galactic latitude with that of the known  $\gamma$ -ray AGN population we find no clear correspondence between these two. However, when comparing the empty fields to the distribution of millisecond and young pulsars, we find a p-value from the two-sided Kolmogorov-Smirnov statistical test of 0.21, which indicates that both distributions could be drawn from the same population. We should note that the empty fields are significantly more concentrated in the Galactic plane, which indicates the presence of a Galactic population of unassociated  $\gamma$ -ray sources with a distribution similar to that of millisecond and young pulsars. No optical or IR localization of a  $\gamma$ -ray source in the empty fields is possible since their localization errors are in a range of arcminutes.

Given the lack of compact radio emission in these 117 2FGL empty fields, we searched existing single dish surveys for large scale radio emission, mainly the Effelsberg 21cm and 11cm surveys focusing on the Galactic plane (Fürst et al. 1990; Reich et al. 1997)<sup>16</sup>. Among the 44 fields that are covered by the Effelsberg surveys, we found 33 fields which had extended structures at or near the  $\gamma$ -ray localization. In many cases structures resembled supernova remnant shells (bubbles). A small representative selection of the structures found in the 11 cm Effelsberg survey is shown in Fig. 6. A qualitative description of those is given below:

- 2FGL J0225.9+6154c: A large scale structure re-

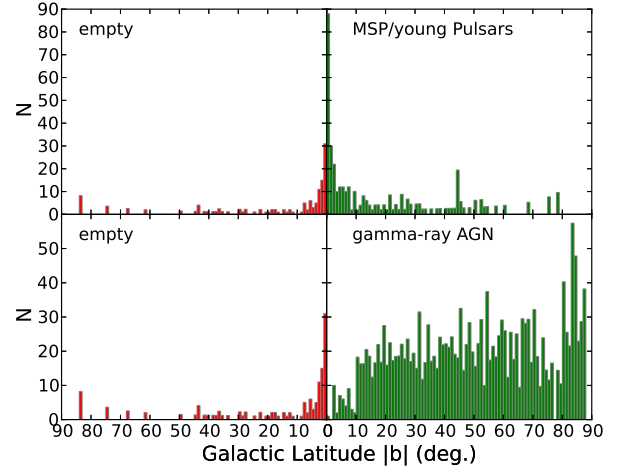


**Figure 5.** Distribution of sources in Galactic latitude  $|b|$  of unassociated 2FGL sources for which no radio point source was found within the  $3\sigma$  confidence localization (red histograms on the left). For comparison, the top right histogram in green shows the Galactic latitude distribution of millisecond pulsars ( $p < 0.01$  s) and young pulsars (age  $< 20,000$  years) extracted from the ATNF pulsar catalog (v1.50; Manchester et al. 2005). In the bottom-right panel the distribution of  $\gamma$ -ray loud AGN from 2LAC (Ackermann et al. 2011) and new AGN associations made in this work is shown. The number counts were divided by  $\cos(|b|)$  to compensate for the change in sky area covered.

sembling a figure of eight with a bright core is found. The  $\gamma$ -ray source is located near the center of this structure. Overall, the structure resembles that of a bipolar outflow around a hot core.

- 2FGL J1746.6-2851c: The  $\gamma$ -ray localization falls onto an arc-like structure resembling that of a supernova remnant shell.
- 2FGL J1924.8+1724c: This  $\gamma$ -ray source lies very close to the innermost region of the Galactic plane. The  $\gamma$ -ray source falls onto an extended radio source of yet unknown origin.
- 2FGL J2019.1+4040: The  $\gamma$ -ray localization falls onto the Northern edge of a sphere-like structure resembling that of a supernova remnant shell.

We also searched the catalog of Galactic supernova remnants (SNR) with radio emission compiled by (Green 2014) that lists 274 known objects for possible matches against the empty fields. We used the known size listed in the Green catalog, and in cases where there is no reliable size used a cone search radius of  $0.2^\circ$ . We found 13 matches among the empty fields leaving still a large fraction of the empty fields spatially unrelated to known SNR. A listing of the matches can be found in Section 3.4. Further investigation of the empty fields that could confirm the nature of the radio structures found is anticipated in the future.

### 3.3. Associations with Compact Sources

Follow-up VLBI observations of 170 selected candidate targets obtained from the VLA and ATCA observations resulted in the detection of compact parsec-scale emission in 95 of the targets. The success rate of detection of parsec-scale emission for sources detected by ATCA was

<sup>16</sup> Image data is available at: <http://www3.mpifr-bonn.mpg.de/survey.html>

**Table 6**

The first 8 rows of 117 2FGL fields for which no radio point source was detected within the  $4\sigma$  localization error at both 5.0/5.5 and 7.3/9.0 GHz. Table 6 is published in its entirety in the electronic edition. A portion is shown here for guidance regarding its form and content.

2FGL	Right Ascension			Declination			l	b	rms	flag
	(h)	(min)	(s)	( $^{\circ}$ )	( $'$ )	( $''$ )	( $^{\circ}$ )	( $^{\circ}$ )	(mJy beam $^{-1}$ )	
J0032.7–5521	00	32	43	–55	21	22	308.5234	–61.5682	0.15/0.19	*
J0038.8+6259	00	38	53	+62	59	48	121.5072	+0.1597	0.083/0.080	*
J0129.4+2618	01	29	29	+26	18	35	133.4507	–35.7836	0.073/0.068	*
J0212.1+5318	02	12	09	+53	18	19	134.9371	–7.6745	0.076/0.074	
J0214.5+6251c	02	14	33	+62	51	11	132.2501	+1.4947	0.078/0.076	*
J0218.7+6208c	02	18	43	+62	08	22	132.9366	+0.9752	0.087/0.083	*
J0225.9+6154c	02	25	59	+61	54	12	133.8172	+1.0463	0.098/0.089	*
J0251.0+2557	02	51	03	+25	57	57	153.9615	–29.6029	0.085/0.078	*

Note: The rms is given for both the 5.5/5.5 and 7.3/9.0 GHz observations. The ‘\*’ flag indicates whether a point source outside of the  $4\sigma$   $\gamma$ -ray localization was found. The ‘e’ flag indicates whether evidence for an extended source was found in the field.

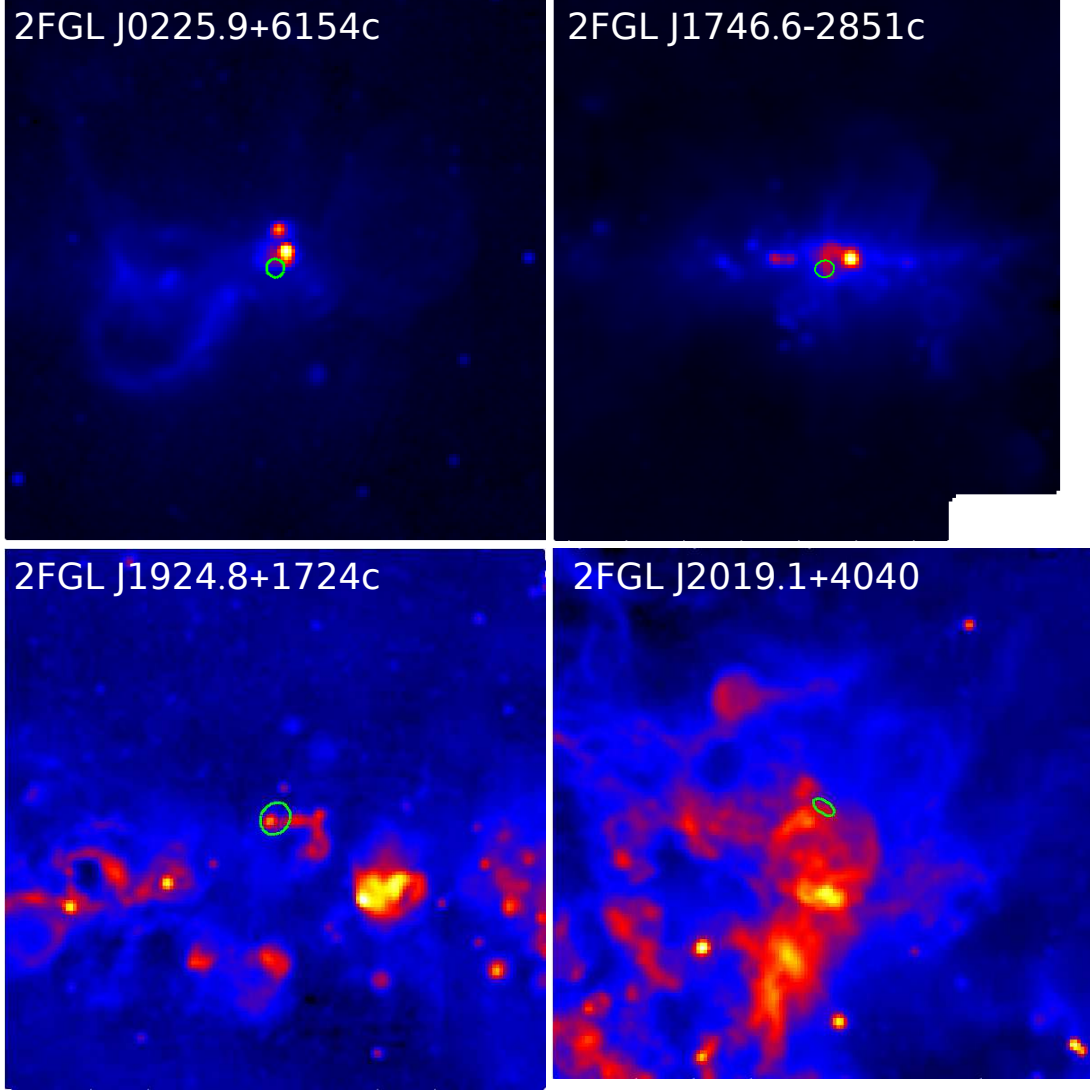


**Figure 6.** Example of four “empty” fields that were observed in the Effelsberg 100m telescope 11cm radio continuum survey of the Galactic plane (Reich et al. 1997; Fürst et al. 1990). The images cover a sky area of 5x5 degrees centered on the four 2FGL sources J0225.9+6154c, J1746.6–2851c, J1924.8+1724c, and J2019.1+4040 respectively. The green circle indicates the  $3\sigma$  localization of the  $\gamma$ -ray point source. The maps are shown in Galactic coordinates (l/b) with no projection applied. In the case of 2FGL J1746.6–2851c not the entire 5x5 degree field was covered by the survey.

54% and for VLA selected targets was 65%. To reliably associate a  $\gamma$ -ray source with a radio source that exhibits parsec-scale radio emission, we use the fact that compact radio sources are relatively rare objects. Their number increases with a decreasing flux density limit. Fitting an empirical relationship for the source counts ( $\log N$ - $\log S$  diagram), we obtain the expected number of compact radio sources with flux densities greater than a given value. Under the assumption of an isotropic distribution of radio sources, we can evaluate the probability of finding a background compact source brighter than a given flux density within the distance  $d$  between a  $\gamma$ -ray source and its possible radio counterpart. Using this probability, we compute the likelihood ratio of association defined as the probability that the radio and  $\gamma$ -ray sources found at a distance  $d$  is physically the same object (and their position difference is due to statistical errors only),  $P_1$ , to the probability that the radio source is a background, unrelated object,  $P_2$ . The first probability is determined as

$$P_1 = e^{-n^2/2} \quad (1)$$

where  $n$  is the normalized distance between the radio and  $\gamma$ -ray source. For the case of a circular error ellipse,  $n = d/\sigma$ . In the general case

$$n = \sqrt{\Delta^2 \alpha \cos^2 \delta + \Delta^2 \delta} \frac{\sqrt{\sigma_{\text{maj}}^2 \sin^2 \beta + \sigma_{\text{min}}^2 \cos^2 \beta}}{\sigma_{\text{maj}} \sigma_{\text{min}}}, \quad (2)$$

where angle  $\beta$  is

$$\beta = \arctan \frac{\Delta \delta}{\Delta \alpha \cos \delta} - (\pi/2 - \theta) \quad (3)$$

and  $\sigma_{\text{maj}}, \sigma_{\text{min}}$  are semi-major and semi-minor axes of the error ellipse, and  $\theta$  is rotation angle of the error ellipse.

Our analysis of the normalized distribution of 1081 arc lengths between reported *Fermi* positions and VLBI positions revealed that the reported parameters of the error ellipse axes should be scaled by a factor of 0.897. We used a rescaled  $\sigma_{\text{maj}}, \sigma_{\text{min}}$  in our analysis. Remarkably, in 2FGL (Nolan et al. 2012), the reported uncertainties were artificially multiplied by a factor of 1.1. Our analysis shows that applying the 1.1 scale factor was an oversight and should be undone.

If we consider the position of a given  $\gamma$ -ray source is precisely known, then the probability to find a background radio source with a given flux density at distance  $d$  or closer is equal to the product of the total number of sources inside an area with radius  $d$  to the total area of the celestial sphere, i.e.

$$P_2 = N(F) \frac{d^2}{4}. \quad (4)$$

According to Petrov et al. (2013), analysis of the complete sample of VLBI detected sources allows us to approximate  $N(F)$  as  $327 \cdot F^{-1.237}$ , where  $F$  is the correlated flux density in Jy at 8 GHz from regions of milliarcsecond size.

If we take into account that the position of a  $\gamma$ -ray source is not precisely known and the probability for a  $\gamma$ -ray photon to be found at a certain location can be

described by a two-dimensional Gaussian distribution, the probability  $P_2$  is expressed via the integral

$$P_2 = N(F) \frac{1}{4\pi \sigma_{\text{maj}} \sigma_{\text{min}}} \int_{-\infty}^{+\infty} \int_{-\infty}^{+\infty} G(\alpha, \delta, \alpha_0, \delta_0, \sigma_{\text{maj}}, \sigma_{\text{min}}) (\Delta^2 \alpha \cos^2 \delta + \Delta^2 \delta) \cos \delta d\alpha d\delta, \quad (5)$$

where  $G(\alpha, \delta, \alpha_0, \delta_0, \sigma_{\text{maj}}, \sigma_{\text{min}})$  is the Gaussian distribution:

$$G(\alpha, \delta, \alpha_0, \delta_0, \sigma_{\text{maj}}, \sigma_{\text{min}}) = \exp \left\{ -\frac{(\Delta \alpha \cos \delta \cos \theta - \Delta \delta \sin \theta)^2}{\sigma_{\text{maj}}^2} - \frac{(\Delta \alpha \cos \delta \sin \theta + \Delta \delta \cos \theta)^2}{\sigma_{\text{min}}^2} \right\}. \quad (6)$$

Expression 5 generalizes equation 4. The probability evaluated with expression 5 is usually greater than evaluated with expression 4.

The likelihood ratio is just

$$\Lambda = \frac{P_1}{P_2}. \quad (7)$$

For 80% of the 2FGL objects the  $1\sigma$  position error is smaller than  $3.6'$ . It follows from Eq. 7 that for these sources if we find a compact radio source brighter than 12 mJy at 8 GHz within their 2FGL  $2\sigma$  error ellipse (semi-major axis  $7.2'$ ), the likelihood ratio of their association is greater than 10. This estimate shows that high resolution radio observations are a very powerful method for establishing an association between radio and  $\gamma$ -ray AGN. The VLBI positions of the detected compact sources, the associated 2FGL field, and their association probability are listed in Table 7. The likelihood ratio shows how much more a true association is likely than spurious association with a background source. For example a value of  $\Lambda = 30$  indicates that the probability that the  $\gamma$ -ray and radio sources are physically related is a factor of 30 greater than the probability they are unrelated. In this case there is a 30:1 chance that it is correct to identify the  $\gamma$ -ray source with the radio source. We accept a likelihood ratio of better than 8.0 as sufficient to claim association of the radio source with the respective  $\gamma$ -ray object. This value was chosen from the distribution of obtained likelihood values. There are 19 detections with a likelihood ratio of less than 8. None had a likelihood ratio between 8.0 and 10.0. Based on this criterion, we have found and associated 76 new  $\gamma$ -ray loud AGN. In the four cases of 2FGL J0253.9+5908, 2FGL J0409.8-0357, 2FGL J1511.8-0513, and 2FGL J1844.3+1548 two high likelihood quasar counterparts were found in each. It is conceivable that both sources contribute to the observed  $\gamma$ -ray emission. We should note that at least one element of these pairs is weak, 11–14 mJy, and the distance between objects is 4–5'. According to Eqn. 4, the probability to find a background source 12 mJy or brighter in a disk of 5' radius is 0.041. Using the binomial distribution, we can evaluate the probability of finding 4 pairs in a random sample of 76 objects: 0.20. This is

**Table 7**

The first 8 rows of 95 VLBI detected radio sources in the fields of 2FGL unassociated  $\gamma$ -ray objects. The full table is available in the supporting documents of the online version of this article. Table 7 is published in its entirety in the electronic edition. A portion is shown here for guidance regarding its form and content.

IAU Name	2FGL	Right Ascension			Declination			S (Jy)	D (")	$N\sigma$	$\Lambda$
		(h)	(min)	(s)	(°)	(')	(")				
J0031+0724	J0031.0+0724	00	31	19.7097	+07	24	53.558	0.0130	3.40	1.29	25.2
J0039+4330	J0039.1+4331	00	39	08.1595	+43	30	14.619	0.0110	1.39	0.55	244.5
J0102+0944	J0102.2+0943	01	02	17.1123	+09	44	09.586	0.0210	1.24	0.47	706.2
J0103+1323	J0103.8+1324	01	03	45.7410	+13	23	45.258	0.0330	0.78	0.25	3366.0
J0116-6153	J0116.6-6153	01	16	19.6126	-61	53	43.514	0.0260	2.68	1.25	100.6
J0157+8557	J0158.6+8558	01	57	03.8159	+85	57	38.873	0.0050	1.75	0.45	60.9
J0221+2514	J0221.2+2516	02	21	26.9651	+25	14	33.665	0.0220	2.82	0.87	111.0
J0223+6821	J0222.7+6820	02	23	04.5374	+68	21	54.995	0.0150	1.97	1.13	109.2

Column description: IAU Name — IAU conforming name; 2FGL — 2FGL identifying name; Right Ascension/Declination — J2000 coordinates of VLBI detection; S — VLBI flux density; D — separation between radio and  $\gamma$ -ray source;  $N\sigma$  — normalized separation between radio and  $\gamma$ -ray source;  $\Lambda$  — likelihood ratio

a fairly high probability. Appearance of multiple associations highlights the nature of the proposed association method: it is statistical, not causal. When we consider a specific object, the probability of false association is always non-zero. But when we consider the population as a whole, we can tolerate a controllable level of spurious associations. In the framework of our method we are in a position to evaluate quantitatively the probability of such a contamination. For the following analysis and discussion we have excluded these four objects that have two counterparts each.

We now compare this new group of radio faint  $\gamma$ -ray loud AGN to the previously known population of  $\gamma$ -ray loud AGN listed as a clean sample in Ackermann et al. (2011, 2LAC). The newly associated  $\gamma$ -ray loud AGN constitutes 8% of the total number of  $\gamma$ -ray associations obtained by combining the 2LAC clean sample with our new detections. In Fig. 7 the  $\gamma$ -ray flux above 100 MeV is plotted against the  $\gamma$ -ray photon index and against the 8 GHz VLBI flux density where available<sup>17</sup> for blazars listed in the 2LAC clean sample and the newly associated  $\gamma$ -ray loud blazars. The newly associated  $\gamma$ -ray loud blazars match very well the general distribution of blazars in the 2LAC clean sample adding to the fainter end of  $\gamma$ -ray loud blazars that are predominantly BL Lac type blazars. This confirms that the newly associated sources are consistent with the previously found general population of  $\gamma$ -ray loud blazars. There are only two new Fermi-AGN associations from our analysis with a flux density above 150 mJy, J2131.0-5417 and J0307.4+4915. This confirms an almost complete sample down to these levels of flux densities. This means that almost no *Fermi* AGN identification with VLBI flux densities greater than 150–200 mJy was previously missed.

### 3.4. Other Associations

Since the release of the 2FGL catalog in 2011 other groups have also attempted to find associations for sources listed as unassociated  $\gamma$ -ray objects. We performed a literature search for unassociated 2FGL objects

<sup>17</sup> For the 2LAC clean sample the rfc-2014b catalog (<http://astrogeo.org/rfc>) was searched using the likelihood ratio for association of  $\gamma$ -ray counterparts with VLBI detections at the 8.0-8.8 GHz band only.

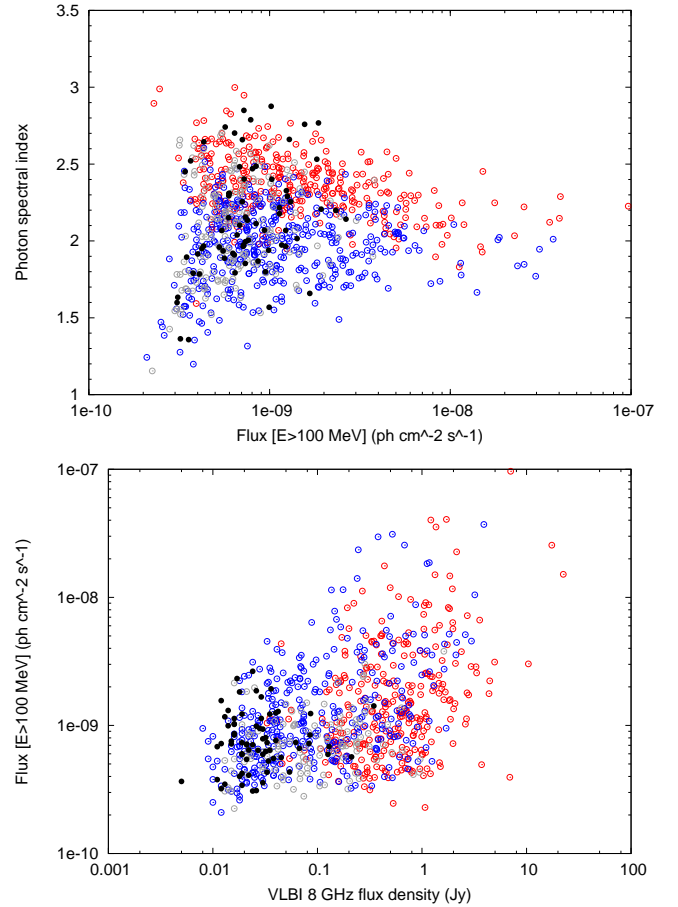


**Figure 7.** *Top:* Photon spectral index plotted against the  $\gamma$ -ray flux above 100 MeV for blazars in the clean 2LAC sample (empty circles) and newly associated blazars (filled black circles). Source classes from the clean sample are indicated by colors, red: FSRQs, blue: BL Lac, grey: AGN of other type. *Bottom:* Distribution of VLBI 8 GHz flux densities of blazars from the clean 2LAC sample (empty circles) and new identifications (black filled circles). The colors are the same as on the left, based on blazar class.

in order to find references on previously reported associations or association attempts. We found that 24 unassociated objects are now associated with Pulsars, 2 are now associated with AGN, and 38 are tentatively asso-



**Table 8**

First 8 entries of 167 possible associations of 2FGL unassociated sources from literature. Table 8 is published in its entirety in the electronic edition. A portion is shown here for guidance regarding its form and content. The source types are: SNR = Supernova Remnant; PSR = Pulsar; XSS = X-ray Binary Star System; BSS = Binary Star System.

2FGL	Association	Type	Reference
J0002.7+6220	G116.9+0.2	SNR?	(Green 2009)
J0106.5+4854	PSR J0106+4855	PSR	(Pletsch et al. 2012)
J0128.0+6330	G126.2+1.6	SNR?	(Green 2009)
J0128.0+6330	G127.1+0.5	SNR?	(Green 2009)
J0214.5+6251c	G132.7+1.3	SNR?	(Green 2009)
J0218.7+6208c	G132.7+1.3	SNR?	(Green 2009)
J0221.4+6257c	G132.7+1.3	SNR?	(Green 2009)
J0224.0+6204	G132.7+1.3	SNR?	(Green 2009)

ciated with or candidates for association with supernova remnants, and two are associated with binary star systems. The corresponding 2FGL identifier, association names, and references are listed in Table 8. The  $\gamma$ -ray source 2FGL J2339.6-0532 was associated with a millisecond pulsar black widow type system, however to date no pulsed  $\gamma$ -ray or radio emission has been detected from this pulsar candidate. Thus it is listed in Table 8 with a ‘?’ as source type together with the relevant reference describing the nature of the possible counterpart at other wavelengths. We also list potential association candidates with Supernova Remnants by cross-matching the list of unassociated sources against the catalog of known Galactic supernova remnants (Green 2014). These entries were marked ‘SNR?’ for their source type. The cross-matching criteria are based on a spatial match, with the  $\gamma$ -ray localization falling within the extent of a listed supernova remnant. If no size is known or the size was marked with a ‘?’ we assumed a size of the SNR of  $0.2^\circ$ . We thus found 96 2FGL sources matching this criteria with 51 unique entries in the Green catalog.

#### 4. DISCUSSION

Our multi-tiered approach observing the localization error circles of unassociated  $\gamma$ -ray sources using radio interferometers led to the association of 76 unassociated  $\gamma$ -ray sources with AGN, reducing the fraction of unassociated sources from 2FGL to 27%. Compared to other association attempts since the release of 2FGL this makes our association method the most successful even compared to searches of pulsed emission among unassociated  $\gamma$ -ray sources. We expect to increase the number of associations with fainter detections of sub-arcsec emission by applying phase referencing calibration on the already obtained data and additional VLBI observations of candidates for association. Additional associations can be expected from planned VLBI observations of Category I sources. Due to selection effects we found significantly more new AGN within  $|b| < 10^\circ$  than what is typical for a uniform distribution of AGN around the sky. This is no surprise, since the focus of most of the association work regarding AGN has been on sky regions of  $|b| > 30^\circ$  and declinations of  $> 10^\circ$ . In Figure 8 the major contributing source classes of identified or associated objects are shown in comparison to the number of unassociated sources, with the newly associated AGN shown in a separate color. Although strictly speaking an AGN

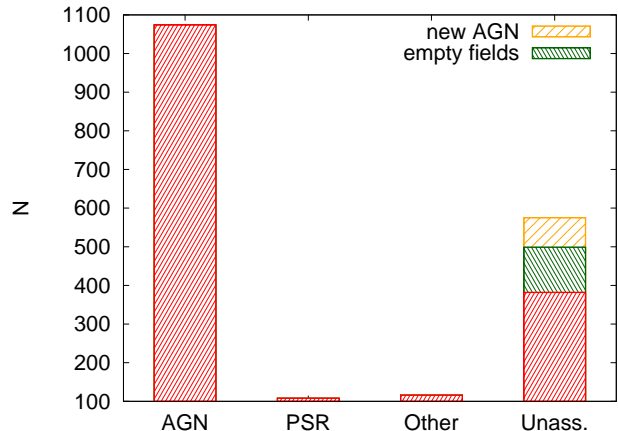


**Figure 8.** The total number of sources listed in 2FGL is 1873, which can be broken down into 1074 AGN, 108 Pulsars (PSR), and 116 other types of sources, e.g. supernova remnants, etc. The 2FGL also listed 575 unassociated sources, for which we found new AGN associations in 76 cases (13% of the unassociated sources). The 117 “empty” fields without association listed make up 20% of the unassociated sources. Since the release of the catalog 28 new associations were reported among the unassociated  $\gamma$ -ray sources.

is not the only type of object with emission at 8 GHz from regions of milliarcsecond scale, the probability of contamination of our sample of associated sources with objects of another type is very low. There are no starburst galaxies with a compact component brighter than 10 mJy detected. To date, only ten radio stars brighter than 10 mJy are known out of the estimated total number of objects with emission from regions of milliarcsecond scales of 100,000.

Radio searches for counterparts at low Galactic latitudes are complicated by the fact that the Galactic plane is bright at radio wavelengths, with contributions from both diffuse emission and bright Galactic sources. For ATCA observations a significant fraction of search regions at low Galactic latitudes were found to have image rms noise levels considerably greater than those of fields at high Galactic latitude. The majority of these were found to be fields in close proximity to Galactic HII regions. At cm wavelengths, HII regions can be very bright (peak brightnesses of tens of Jy beam $^{-1}$ ) and as much as 5–10' in extent, and so the  $\gamma$ -ray search field can be contaminated by radio emission from an HII region in the primary beam or one of the side-lobes. Paladini et al. (2003) compiled a catalog of 1442 Galactic HII regions from previously published lists, and the number of known HII regions has been further expanded by Giveon et al. (2005), with the addition of more compact regions, and Anderson et al. (2014), among others. The presence of such sources near search fields makes searches for faint radio counterparts more difficult. A thorough analysis of HII regions in this context is anticipated in the future.

We find that a significant fraction of radio observations around unassociated  $\gamma$ -ray sources resulted in non-detections of a single radio source within  $3\sigma$  of the localization down to a detection limit of  $\sim 1$  mJy. These empty fields were shown to be concentrated in the Galactic plane, especially within the inner  $2^\circ$  in Galactic latitude (see Fig. 9). The spatial distribution of empty fields is compatible with that of young pulsars and millisecond pulsars, which are known to produce  $\gamma$ -ray emis-

sion. A look at existing single dish survey maps revealed that 75% of those empty fields covered by the Effelsberg Galactic plane survey show extended radio emission with some of them resembling supernova remnant shells. We searched the catalog of Galactic SNRs (Green 2014) and found only 13 matches, while a search over all unassociated  $\gamma$ -ray sources resulted in 96 spatial matches with known SNRs. Thus, there seems to be no systematic preference for finding spatial matches with SNRs in empty fields. However, we note that the search of the Green catalog is heavily biased toward the innermost region of the Galactic plane and lacks SNR detections at separations larger than a few degrees from the plane. A systematic study of existing surveys probing large scale radio structures in combination with higher sensitivity new single-dish and interferometric observations with short baselines have the potential to shed more light on the nature of radio emission found in those empty fields and whether it can be related to any known class of objects that are candidates for  $\gamma$ -ray production such as supernova remnants. This will be investigated in a future publication.

In addition, pulsars typically show  $\gamma$ -ray photon indices below 1.8, however we only found two empty fields with photon indices below 1.8. The average photon index found is 2.34, which is consistent with the average spectral index of flat spectrum radio quasars (FSRQ) and supernova remnants. However, FSRQs are not expected to be very abundant at the probed  $\gamma$ -ray luminosities, as can be inferred from Fig. 7. The 83 identified pulsars listed in 2FGL have an average photon spectral index of  $1.37 \pm 0.44$ , which is also incompatible with the distribution found for the empty fields. Thus, we suggest that a large fraction of the empty fields are either related to emission from supernova remnants, possibly interacting with star forming clouds in their vicinity, or a new unexpected Galactic population of  $\gamma$ -ray emitters. The fraction of empty fields among all unassociated  $\gamma$ -ray sources is indicated in Fig. 8.

In addition to the empty fields we found an abundance of sources concentrated in the Galactic plane even among those  $\gamma$ -ray sources for which we found radio sources within  $3\sigma$  of their localization but for which no compact AGN emission was detected. Both the distribution of empty fields and the location of new radio sources is biased by the selection effect that unassociated  $\gamma$ -ray sources are concentrated within the inner  $30^\circ$  of the Galactic plane. However, we suggest that such a Galactic population could also be related to emission from pulsars. Lazio & Cordes (2008) have shown that in dense regions of the Galactic plane, scatter broadened pulsed radio emission can be detected in continuum observations up to several GHz and could provide a significant contribution to the radio sources that were found in this survey. We also consider scatter broadening as a possible reason for a lack of non-detections of compact emission in the Galactic plane. In order to test this, we take the complete sample of known AGN detected by VLBI at 8 GHz above 180 mJy as listed in the radio fundamental catalog (rfc-2014b) and compare the source densities within  $\pm 10^\circ$  of the Galactic plane. We found that within the Galactic plane the source density is  $5.9 \cdot 10^{-2} \text{ deg}^{-2}$  compared to outside the Galactic plane where the source

density is  $7.0 \cdot 10^{-2} \text{ deg}^{-2}$ . Thus scatter broadening does not seem to play a significant role for VLBI detections and thus is not able to explain the lack of AGN  $\gamma$ -ray associations within the Galactic plane which supports the presence of a new Galactic population of  $\gamma$ -ray sources not yet associated. A more thorough study of this effect is anticipated in future work focusing on the VLBI detections of all known  $\gamma$ -ray loud AGN.

We note that our search in the literature of reported associations and a spatial cone search of the Green catalog showed that in the case of 2FGL J0553.9+3104 an association was made with PSR J0554+3107 and a spatial match was found with SNR G179.0+2.6. In addition, we obtained a high likelihood association ( $\Lambda = 53.1$ ) with the AGN J0553+3106. In three other cases (2FGL J0538.1+2718, J0641.1+1006c, and J2041.5+5003) where we found a spatial match with a SNR from the Green catalog we also report a high confidence association with an AGN. Thus, a spatial search among known supernova remnants produced a possible 3% false positive rate among the unassociated  $\gamma$ -ray sources suggested to be related with supernova remnants. A more robust method has to be developed in order to claim association with a supernova remnant. We should note that the presence of an AGN or a supernova remnant is not necessarily mutually exclusive and the  $\gamma$ -ray emission is potentially a combination from both sources in the respective fields. This shows the importance for a search of AGN among  $\gamma$ -ray sources in the Galactic plane in order to identify fields that have multiple  $\gamma$ -ray sources contributing to the observed high energy emission.

Fujinaga, Y., Niinuma, K., Fijisawa K. et al. (2014, submitted) presented at the European VLBI Symposium 2014 in October 2014 preliminary results of their independent program for observing 845 sources in the vicinity of 231 2FGL unassociated sources. They have detected 28 sources with VLBI. We confirm 19 of their detections.

#### 4.1. Comparison with indirect methods of association using continuum radio spectra

The spectrum of synchrotron radiation from a source at parsec-scales detected with VLBI is usually flat or inverted. The spectra at kiloparsec scales have a significant contribution of the emission that gives results from an interaction of a jet with interstellar or the intergalactic medium and thus are usually steep. Emission from a compact region dominates for flat-spectrum sources and emission from extended regions dominates for steep-spectrum objects, although there exists a considerable number of exceptions in both cases. The  $\gamma$ -ray emission detected from AGN is most likely related to the AGN core emission, due to a similar boosting of  $\gamma$ -rays and radio emission with common Doppler factors under small observing angles.

The spectrum of a radio source is often cited as a criteria that helps to associate it with a  $\gamma$ -ray source. We collected information about the spectrum of radio sources using the CATS database<sup>18</sup>. That database contains over 200 radio catalogs. Cross-matching these catalogs, we computed spectral indices of sources from observations at low resolution (10–100"). The results are presented in Table 9. We should bear in mind that these spectra are

<sup>18</sup> [http://cats.sao.ru/doc/CATS\\_list.html](http://cats.sao.ru/doc/CATS_list.html)

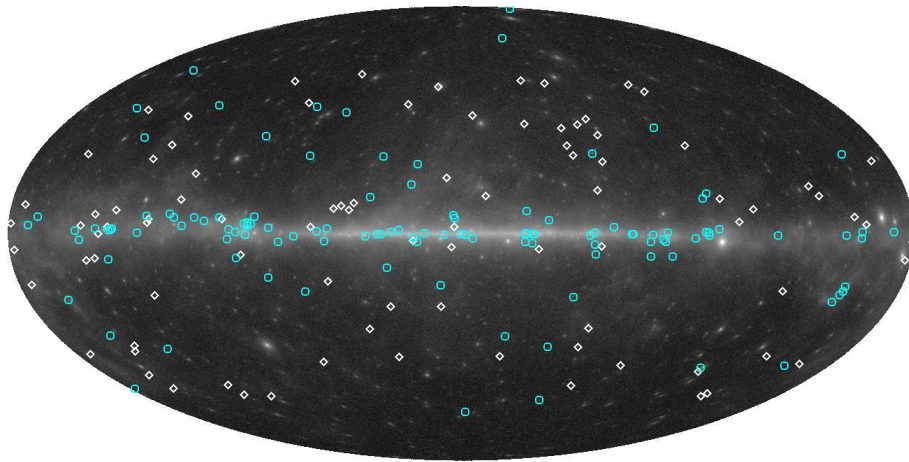


**Figure 9.** The *Fermi* two-year all-sky map for energies above 1 GeV (Credit: NASA/DOE/Fermi LAT Collaboration). The positions of empty fields are marked with cyan circles and the positions of newly associated AGN are marked with white diamonds.

**Table 9**

Spectrum of *Fermi* associations with AGN confirmed with VLBI.

Flat spectrum sources:	830 (83%)	$\alpha > -0.5$	$S \sim S^\alpha$
Steep spectrum sources:	74 (7%)	$\alpha < -0.5$	
Unknown spectrum:	101 (10%)		

compiled from non-simultaneous data and thus may be distorted by source variability.

Indeed,  $\sim 90\%$  of *Fermi* associations with AGN confirmed with VLBI have a spectral index flatter than  $-0.5$ . Among 76 associations found in the present paper 67 objects have a flat spectrum, 7 have a steep spectrum, and for two objects the spectral index has not been reliably determined. Of the 75 sources that were not detected in our VLBI observations, 53% were flat-spectrum sources, 33% were steep-spectrum sources, and others were without known spectral index. If one wants to achieve completeness then VLBI observations should be performed ignoring prior spectral information.

If a source has a flat radio spectrum, this does not automatically imply it is an AGN or is associated with a  $\gamma$ -ray object. A number of planetary nebulae and HII compact regions show flat spectra as well. Since flat spectrum sources were predominantly observed in prior VLBI surveys, there is a certain selection bias that results in under-representation of steep spectrum sources. The spectrum of a source at low resolution does not reveal the nature of a source itself, but can serve as a proxy to make a rough estimate of the expected flux density from a compact component. However, the value of information about source spectrum is rather limited for population analysis since the ratio of flux density of a core to the flux density at kilo-parsec scales has a significant spread even for flat-spectrum sources. At the same time, this ratio is significantly higher than for the steep-spectrum sources. It is difficult to evaluate quantitatively the probability of a *Fermi* association using only estimates of flux density at low resolution and a spectral index. However, in a situation when observing resources are limited, reducing the list of sources to be observed with VLBI by their pre-selection on basis of the spectra, if such information is available, increases the number of detections.

#### 4.2. Comparison with indirect methods of association using IR colors

Massaro et al. (2011) cross-matched *Fermi* sources associated with AGN with the WISE catalog (Wright et al. 2010) and found that matches occupy a distinctive zone in the color-color diagram  $[3.4]-[4.6] \mu\text{m}$  versus  $[4.6]-[12] \mu\text{m}$ . This prompted them to suggest that this feature can be used for association of *Fermi* sources with blazars. In numerous papers they claim their method provides an association with a probability of false association of just 3–4%. In particular, in Massaro et al. (2013) they investigated two samples: NVSS and SUMSS sample of 324 unassociated *Fermi* sources (containing 56% of unassociated 2FGL sources) and a sample of 411 sources that we have observed in the first ATCA campaign. They proposed a number of associations.

In Table 10 we summarize and compare our statistics with that presented in Massaro et al. (2013). We see that the Massaro et al. method, first, significantly under-predicts associations with AGN, second, a significant number of its predictions are not confirmed with VLBI. We should note, that to date, we have followed-up with VLBI only 1/2 of our targets, and the actual number of associations with *Fermi* is expected to be higher. This discrepancy prompted us to perform our own analysis of the WISE color-color diagram using the ALLWISE catalog (Mainzer et al. 2011).

First, we selected a sample of *Fermi* associations with AGN confirmed with VLBI with the likelihood ratio greater than 10. In total, 1005 sources fit this criteria. Among them, 959 objects have an association with a source from the ALLWISE catalog that have been detected at both 3.4, 4.6, and 12  $\mu\text{m}$  within 5'' of a VLBI position. We find that *Fermi* sources are associated with predominantly bright ALLWISE objects: 97% of the *Fermi* sources have a magnitude of less than 16.25 at 3.4  $\mu\text{m}$  and 15.25 at 4.6  $\mu\text{m}$ , well below the completeness level of ALLWISE. We discarded fainter ALLWISE objects for further analysis. We build a color-color diagram of differences in magnitude  $[3.4]-[4.6] \mu\text{m}$  versus  $[3.4]-[12] \mu\text{m}$  (Figure 10). The population of *Fermi* sources are indeed concentrated within a particular region. We noticed that *Fermi* sources concentrate along two ellipses in the modified diagram  $([3.4]-[4.6])^2 \mu\text{m}$  ver-



**Table 10**

Performance of the different association methods. The column labeled “predicted” is that of the Massaro et al. method; the “confirmed” number is the number of Massaro et al. predictions that we have confirmed with VLBI; the false associations column is the number of Massaro et al. predictions we can refute, because we found another counterpart with high likelihood ratio; the VLBI number is the number of VLBI detections (i.e., confirmed AGN) in the sample.

	sample size	predicted	confirmed	false assoc.	VLBI
NVSS+SUMSS sample	324	52	30	2	95
ATCA#1 sample	411	11	3	1	51

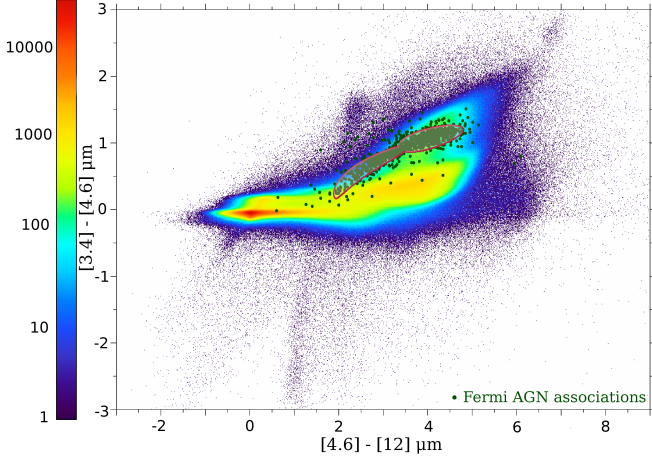


**Figure 10.** Color-color diagram of bright ALLWISE sources. Logarithm of source density is shown with color map. *Fermi* sources associated with AGN with the likelihood ratio  $> 10$  are shown with green circles. The area of *Fermi* associations is shown with a red contour.

sus  $[3.4] - [12] \mu\text{m}$ . Therefore, we modeled the region with high concentration of *Fermi* sources with two 4th order figures that obey equations of

$$\frac{(x - x_o)^2}{a^2} + \frac{(y - y_o)^4}{a^4(1 - e^2)^2} = 1$$

rotated counter-clockwise at angle  $\zeta$ . Parameters of the figures:  $x_{o1} = 1.90, y_{o1} = 0.05, a_1 = 1.00, e_1 = 0.99, \zeta_1 = 27^\circ; x_{o2} = 3.42, y_{o2} = 0.88, a_2 = 0.78, e_2 = 0.92, \zeta_2 = 24^\circ$ . These figures capture 81% of *Fermi* sources with counterparts in the WISE catalog.

The area of *Fermi* associations contains 777 out of 959 sources, i.e. 3/4 of the  $\gamma$ -ray objects that have associations with ALLWISE and have data at 3.4, 4.6 and 12  $\mu\text{m}$ . The area contains 1.2 million ALLWISE bright objects out of 68.5 millions. Only 0.06% of them are known  $\gamma$ -ray sources. On average, 1.1 ALLWISE sources from the *Fermi* association area can be found in any field of radius  $7.2'$  that is within the upper limit  $2\sigma$  error ellipse for 80% of the *Fermi* sources, i.e. the probability to find at least one background source is 67%. This rules out using the color-color diagram for a meaningful association without additional information.

Massaro et al. suggested using the association with the lower frequency radio catalogs NVSS or SUMSS. Almost all known *Fermi* associations with AGN are present in the NVSS or SUMSS catalogs. Since the number of sources in radio catalogs is several orders of magnitude fewer than there are in WISE, pre-selection of only those WISE sources that have a counterpart in catalogs with frequencies below 5 GHz allows one to improve the predictive power of the WISE color-color diagram. We se-

**Table 11**

First two rows: statistics of NVSS sources brighter 10 mJy at 1.4 GHz with  $\delta > -40^\circ$  in the zone of Galactic plane and in the zone beyond the Galactic plane. Last two rows: statistics of *Fermi* sources in these zones.

	$ b  > 10^\circ$	$ b  < 10^\circ$
Total number	478,808	102,288
# of ALLWISE counterparts	84,747	24,818
# sources in the $\gamma$ -ray AGN area	20,229	1,885
Total # of 2FGL sources	791	89
# of 2FGL sources in the $\gamma$ -ray AGN area	615	56

**Table 12**

Statistics of two samples of radio sources found within  $2\sigma$  error ellipses of *Fermi* unidentified sources. Second column: sample of NVSS and SUMSS sources brighter than 10 mJy at 1.4 and 0.8 GHz respectively. Third column: sample of sources brighter than 10 mJy at 5–9 GHz from our dedicated ATCA and VLA surveys.

	NVSS+SUMSS	ATCA+VLA
Total number	1627	275
# of ALLWISE counterparts	431	160
# sources in $\gamma$ -ray AGN area	96	64
# VLBI observed sources	44	42
# VLBI detected sources	43	41

lected NVSS sources brighter than 10 mJy at 1.4 GHz—the NVSS catalog is complete at the level of 4 mJy—and counted the number of sources with bright ALLWISE counterparts and among them, the number of sources that fall within the *Fermi* association area. The results are summarized in Table 11. We note, the statistics are different whether or not the Galactic plane is included. Within  $10^\circ$  of the Galactic plane 7.6% of the sources have colors that fall in the  $\gamma$ -ray AGN area, while the share of these sources is a factor of 3 greater if we consider sources further than  $10^\circ$  of the Galactic plane. We attribute this disparity to a greater share of Galactic objects visible with both NVSS and ALLWISE at low Galactic latitudes. Within the Galactic plane, 1.8% of NVSS sources with colors in the  $\gamma$ -ray AGN area account for 62% of the associations, and 4.2% of the NVSS sources with  $|b| > 10^\circ$  with colors in the same area account for 78% of the associations.

We performed a search for sources with colors in the  $\gamma$ -ray AGN area for two samples: a) NVSS and SUMSS sources brighter than 10 mJy at 1.4 and 0.8 GHz respectively within  $2\sigma$  error ellipse of all 2FGL unidentified sources; and b) ATCA and VLA sources from our program that are brighter than 10 mJy at any sub-band within 5–9 GHz. We restricted the flux density because weaker sources are not reliably associated using our method. The results are shown in Table 12.

First, we should note that among our 95 VLBI detected sources, 76 are confirmed associations. However among those sources only 41 fall within the  $\gamma$ -ray area of the color-color diagram. Thus, the method of identifying AGN counterparts of *Fermi* sources using their IR colors misses one half of the objects. At the same time, analysis of the entire sample of confirmed radio-counterparts showed that only 3/4 of the sources have IR colors in the  $\gamma$ -ray AGN area. This discrepancy can be explained by either an unintended bias in our VLBI observation program or by a greater share of sources that are not found in the  $\gamma$ -ray AGN area among radio weak sources, since the sources that we have observed in our program are systematically weaker. We see the detection rate of sources selected on the basis of flux density at 5–9 GHz and IR colors is exceptionally high, more than 95%, unlike what would be expected.

It is worth mentioning that among 9,100 AGN detected in VLBI surveys only 30% lie in the AGN area of the IR color-color diagram in contrast to 77% of AGN that have detectable  $\gamma$ -ray emission. This implies that the color-color diagram confines not the AGN population in general, but a specific sub-class of AGN.

To summarize, the main differences between our method of association and the method of Massaro et al. are 1) we provide a quantitative measure for association confidence: the likelihood ratio; 2) the Massaro et al. color-color method misses half of the sources for which we find associations, however they only focused on the population of  $\gamma$ -ray blazars and not all types of AGN as we do; 3) our method allows us to build a flux-limited sample of associations suitable for population studies.

## 5. SUMMARY AND CONCLUSIONS

We present a catalog of radio sources resulting from an all-sky radio survey between 5 and 9 GHz of fields surrounding the localization of all unassociated  $\gamma$ -ray sources listed in the *Fermi* Large Area Telescope Second Source Catalog. In total we found 865 radio sources which could be considered as candidates for association. Follow-up observations with VLBI on 170 selected from those candidates led to the firm association of 76 previously unknown  $\gamma$ -ray AGN. We provide the likelihood ratio for each association.

In addition, among the 588 unassociated  $\gamma$ -ray sources targeted, we found that in 129 not a single radio source was found above the detection limit of our observations within the  $3\sigma$  localization error of the  $\gamma$ -ray sources. These “empty” fields were found to be particularly concentrated around the innermost region of the Galactic plane and we suggest them to be associated with a previously unknown Galactic population of  $\gamma$ -ray emitters.

We compare our method of direct radio observations with indirect methods of association based on IR colors as suggested by Massaro et al. We have confirmed one half of their associations. We find that other VLBI detected sources occupy a different place in the IR color-color diagram and thus cannot be associated with AGN using only their IR colors. This finding demonstrates the practical limit of the indirect method.

Compared with other published results of  $\gamma$ -ray source association, our approach appears to be the most productive for establishing AGN associations. We plan to continue radio observations of unassociated sources that

will be discovered in subsequent releases of the *Fermi* source catalog

We thank Dave McConnell for his support with the ATCA observations. We thank members of the *Fermi* collaboration, in particular Francesco Massaro, Jean Ballet, and Elizabeth Ferrara, for useful discussions. We thank Dave Green, Heinz Andernach, and the anonymous referee for useful discussions, corrections, and comments that have significantly improved the quality of this publication. We thank NASA for support under FERMI grant NNX12A075G. YYK was partly supported by the Russian Foundation for Basic Research (project 13-02-12103) and the Dynasty Foundation. The National Radio Astronomy Observatory is a facility of the National Science Foundation operated under cooperative agreement by Associated Universities, Inc. The Australia Telescope Compact Array / Long Baseline Array are part of the Australia Telescope National Facility which is funded by the Commonwealth of Australia for operation as a National Facility managed by CSIRO. This publication makes use of data products from the Wide-field Infrared Survey Explorer, which is a joint project of the University of California, Los Angeles, and the Jet Propulsion Laboratory/California Institute of Technology, and NEOWISE, which is a project of the Jet Propulsion Laboratory/California Institute of Technology. WISE and NEOWISE are funded by the National Aeronautics and Space Administration. This work made use of the Swinburne University of Technology software correlator, developed as part of the Australian Major National Research Facilities Programme and operated under licence. This research has made use of NASA’s Astrophysics Data System and has made use of the NASA/IPAC Extragalactic Database (NED) which is operated by the Jet Propulsion Laboratory, California Institute of Technology, under contract with the National Aeronautics and Space Administration. This research has made use of data, software and/or web tools obtained from NASA’s High Energy Astrophysics Science Archive Research Center (HEASARC), a service of Goddard Space Flight Center and the Smithsonian Astrophysical Observatory, of the SIMBAD database, operated at CDS, Strasbourg, France, and the TOPCAT software version 4.1<sup>19</sup> (Taylor 2005). The authors made use of the database CATS (Verkhodanov et al. 2007) of the Special Astrophysical Observatory.

*Facilities:* VLA, VLBA, ATCA, LBA, FERMI (LAT).

## REFERENCES

- Abdo, A. A., Ackermann, M., Ajello, M., et al. 2009, *ApJS*, 183, 46
- . 2010, *ApJS*, 188, 405
- Ackermann, M., Ajello, M., Allafort, A., et al. 2011, *ApJ*, 743, 171
- . 2013, *ApJS*, 209, 34
- Anderson, L. D., Bania, T. M., Balser, D. S., et al. 2014, *ApJS*, 212, 1
- Beasley, A. J., Gordon, D., Peck, A. B., et al. 2002, *ApJS*, 141, 13
- Bock, D. C.-J., Large, M. I., & Sadler, E. M. 1999, *AJ*, 117, 1578
- Briggs, D. S. 1995, PhD thesis, The New Mexico Institute of Mining and Technology
- Casandjian, J.-M., & Grenier, I. A. 2008, *A&A*, 489, 849
- Clark, B. G. 1980, *A&A*, 89, 377
- Condon, J., Darling, J., Kovalev, Y. Y., & Petrov, L. 2011, *ArXiv e-prints*, arXiv:1110.6252

<sup>19</sup> [http://www.star.bris.ac.uk/\\$\sim\\$mbt/topcat/](http://www.star.bris.ac.uk/$\sim$mbt/topcat/)

- Condon, J. J., Cotton, W. D., Greisen, E. W., et al. 1998, *AJ*, 115, 1693
- Deller, A. T., Briskin, W. F., Phillips, C. J., et al. 2011, *PASP*, 123, 275
- Fomalont, E. B., Petrov, L., MacMillan, D. S., Gordon, D., & Ma, C. 2003, *AJ*, 126, 2562
- Fürst, E., Reich, W., Reich, P., & Reif, K. 1990, *A&AS*, 85, 805
- Giveon, U., Becker, R. H., Helfand, D. J., & White, R. L. 2005, *AJ*, 129, 348
- Green, D. A. 2009, *Bulletin of the Astronomical Society of India*, 37, 45
- . 2014, *ArXiv e-prints*, arXiv:1409.0637
- Greisen, E. W. 1990, in *Acquisition, Processing and Archiving of Astronomical Images*, ed. G. Longo & G. Sedmak, 125–142
- Hambly, N. C., MacGillivray, H. T., Read, M. A., et al. 2001, *MNRAS*, 326, 1279
- Kovalev, Y. Y. 2009, *ApJL*, 707, L56
- Kovalev, Y. Y., Petrov, L., Fomalont, E. B., & Gordon, D. 2007, *AJ*, 133, 1236
- Lazio, T. J. W., & Cordes, J. M. 2008, *ApJS*, 174, 481
- Mainzer, A., Bauer, J., Grav, T., et al. 2011, *ApJ*, 731, 53
- Manchester, R. N., Hobbs, G. B., Teoh, A., & Hobbs, M. 2005, *AJ*, 129, 1993
- Massaro, F., D’Abrusco, R., Ajello, M., Grindlay, J. E., & Smith, H. A. 2011, *ApJL*, 740, L48
- Massaro, F., D’Abrusco, R., Paggi, A., et al. 2013, *ApJS*, 206, 13
- Mauch, T., Murphy, T., Buttery, H. J., et al. 2003, *MNRAS*, 342, 1117
- Murphy, T., Mauch, T., Green, A., et al. 2007, *MNRAS*, 382, 382
- Nolan, P. L., Abdo, A. A., Ackermann, M., et al. 2012, *ApJS*, 199, 31
- Paladini, R., Burigana, C., Davies, R. D., et al. 2003, *A&A*, 397, 213
- Petrov, L. 2011, *AJ*, 142, 105
- . 2012, *MNRAS*, 419, 1097
- . 2013, *AJ*, 146, 5
- Petrov, L., Gordon, D., Gipson, J., et al. 2009, *Journal of Geodesy*, 83, 859
- Petrov, L., Kovalev, Y. Y., Fomalont, E., & Gordon, D. 2005, *AJ*, 129, 1163
- Petrov, L., Kovalev, Y. Y., Fomalont, E. B., & Gordon, D. 2006, *AJ*, 131, 1872
- . 2008, *AJ*, 136, 580
- . 2011a, *AJ*, 142, 35
- Petrov, L., Mahony, E. K., Edwards, P. G., et al. 2013, *MNRAS*, 432, 1294
- Petrov, L., Phillips, C., Bertarini, A., Murphy, T., & Sadler, E. M. 2011b, *MNRAS*, 414, 2528
- Petrov, L., & Taylor, G. B. 2011, *AJ*, 142, 89
- Pletsch, H. J., Guillemot, L., Allen, B., et al. 2012, *ApJ*, 744, 105
- Reich, P., Reich, W., & Furst, E. 1997, *A&AS*, 126, 413
- Taylor, G. B., Healey, S. E., Helmboldt, J. F., et al. 2007, *ApJ*, 671, 1355
- Taylor, M. B. 2005, in *Astronomical Society of the Pacific Conference Series*, Vol. 347, *Astronomical Data Analysis Software and Systems XIV*, ed. P. Shopbell, M. Britton, & R. Ebert, 29
- Tingay, S. J., Murphy, D. W., & Edwards, P. G. 1998, *ApJ*, 500, 673
- Verkhodanov, O., Trushkin, S., Andernach, H., & Chernenkov, N. 2007, *Highlights of Astronomy*, 14, 636
- Wright, E. L., Eisenhardt, P. R. M., Mainzer, A. K., et al. 2010, *AJ*, 140, 1868